Spin-up of stratified rotating flows at large Schmidt number: experiment and theory

By R. E. HEWITT[1,2], P. A. DAVIES[2], P. W. DUCK[1],
AND M. R. FOSTER[3]

[1] Department of Mathematics, University of Manchester,
Oxford Road, Manchester, M13 9PL, UK

[2] Department of Civil Engineering, The University,
Dundee, DD1 4HN, UK

[3] Department of Aerospace Engineering, Applied Mechanics and Aviation,
The Ohio State University, Columbus, OH, 43210, USA

We consider the nonlinear spin-up/down of a rotating stratified fluid in a conical container. An analysis of axisymmetric similarity-type solutions to the relevant boundary-layer problem, Duck, Foster & Hewitt (1997), has revealed three types of behaviour for this geometry. In general, the boundary layer evolves to either a steady state, or a gradually thickening boundary layer, or a finite-time singularity depending on the Schmidt number, the ratio of initial to final rotation rates, and the relative importance of rotation and stratification.

In this paper we emphasize the experimental aspects of an investigation into the initial readjustment process. We make comparisons with the previously presented boundary-layer theory, showing good quantitative agreement for positive changes in the rotation rate of the container (relative to the initial rotation sense). The boundary-layer analysis is shown to be less successful in predicting the flow evolution for nonlinear decelerations of the container. We discuss the qualitative features of the spin-down experiments, which, in general, are dominated by non-axisymmetric effects. The experiments are conducted using salt-stratified solutions, which have a Schmidt number of approximately 700.

The latter sections of the paper present some stability results for the steady boundary-layer states. A high degree of non-uniqueness is possible for the system of steady governing equations; however the experimental results are repeatable and stability calculations suggest that 'higher branch' solutions are, in general, unstable. The eigenvalue spectrum arising from the linear stability analysis is shown to have both continuous and discrete components. Some analytical results concerning the continuous spectrum are presented in an appendix.

A brief appendix completes the previous analysis of Duck, Foster & Hewitt (1997), presenting numerical evidence of a different form of finite-time singularity available for a more general boundary-layer problem.

1. Introduction

The readjustment (spin-up) of a rotating fluid subsequent to an abrupt change in the rotation rate of the bounding walls is a fundamental problem that has both geophysical and industrial relevance. The spin-up problem for homogeneous fluids

has received a great deal of attention; see for example Greenspan & Howard (1963), Greenspan (1968), Benton & Clark (1974), Wedemeyer (1964) and Greenspan & Weinbaum (1965). The level of interest can perhaps be attributed, apart from obvious practical applications, to an ability to pose the problem in terms of a very simple geometry. The linear analysis of Greenspan & Howard (1963) showed that the influence of the container geometry was minimal, and that the essential physical mechanisms are present in the unbounded flow between two infinite parallel planes.

After an impulsive change (which is assumed to be small relative to the initial rotation) in the rotation rate of the container walls (a circular, cylindrical container for example), Ekman layers form on the horizontal boundaries within the time taken for one rotation of the container. For an Ekman number $E = v/\Omega h^2$, where v is the kinematic viscosity of the fluid, Ω a typical angular frequency and h an appropriate lengthscale, the timescale for a bulk readjustment of a homogeneous fluid to the new conditions is $E^{-1/2}\Omega^{-1}$. This 'fast' spin-up is attributed to the mass flux in the boundary layer, caused by an imbalance between viscous, centrifugal and pressure forces, the final result of which is a secondary, meridional circulation. The recirculation of fluid from the Ekman layers via the sidewall layers† gradually decays as the angular frequency of the interior fluid begins to approach that of the final state. The last stage of spin-up is then completed by a viscous decay of any residual motion.

The later theories of Greenspan & Weinbaum (1965) and Wedemeyer (1964) treated the global, nonlinear spin-up problem for a homogeneous fluid. Nonlinear effects can drastically alter the spin-up behaviour; Wedemeyer (1964) and Greenspan (1968) discuss cases (of spin-up from rest) in which the sidewall shear layer can become detached, propagating into the interior towards the axis of rotation.

Nonlinear Ekman layers have also been discussed extensively for the case of a swirling flow above an infinite rotating disk, Rogers & Lance (1960). For this geometry the radial dependence can be removed in a manner first proposed by von Kármán, reducing the governing system to ordinary differential equations without neglecting any terms in the Navier–Stokes equations (thus providing an exact solution). The qualitative features of the nonlinear Ekman layer are comparable with those provided by the linear analysis. Simple approximations to nonlinear results obtained from steady solutions to the boundary-layer equations have been used to provide an Ekman compatibility condition, thus allowing the development of interior solutions, Wedemeyer (1964), that are consistent with the Ekman suction/blowing required by the boundary layers.

The next obvious extension to the large body of work concerning spin-up mechanisms was to include the effect of density stratification. Attention has centred on the problem of spin-up within a circular cylinder (for both multi-layer and linear density gradients), with some debate over the results of the initial investigators. A theoretical analysis of the linear spin-up process for a stably stratified fluid was presented by Holton (1965), which proved to be qualitatively correct but had some inaccuracies in the treatment of the sidewall layer. The boundary layer on the vertical (generally all the investigators assumed an axis of rotation parallel to the direction of local gravitational acceleration) sidewall of the cylinder plays a distinctly different role in the stratified spin-up problem. In particular, because buoyancy forces inhibit vertical motion, the mass transport from the horizontal Ekman layers (which obviously remain free from any direct buoyancy influence) cannot be accepted by an insulated

---

† Or equivalently for the case of two parallel disks, the Ekman transport forces a radial flow from infinity to satisfy a continuity of mass constraint in the interior.

sidewall layer. This character of the flow near the vertical walls was pointed out in a later paper by Pedlosky (1967), but he incorrectly predicted that spin-up would then be achieved by a diffusive mechanism. The correct description of the linear spin-up process was later presented by Walin (1969) and Sakurai (1969), who predicted that the effect of the stable stratification was to restrict the recirculation of fluid from the Ekman layers to a localized region near to the horizontal boundaries (without requiring transport into the sidewall layers in agreement with Pedlosky). The result of this localized spin-up is a quasi-steady state, which has a linear shear in the horizontal velocity component.

The recirculation process and penetration of the fluid ejected from the Ekman layers into the interior flow is governed by the ratio of the frequencies due to buoyancy and rotational inertia, as determined by the Burger number; this is defined as $S = N^2/\Omega^2$, where $N^2 = -(g/\rho_o)\, \mathrm{d}\bar{\rho}(z)/\mathrm{d}z$ is the Brunt–Väisälä frequency (ρ_o and $\bar{\rho}(z)$ are a reference density and stable linear stratification respectively and z is a vertical coordinate). This localized readjustment near to the horizontal boundaries eventually ceases as the difference in (local) angular frequency between the Ekman layer and adjacent fluid decreases. Therefore, a quasi-steady localized spin-up is achieved on the fast $E^{-1/2}\Omega^{-1}$ timescale with a reduction to solid-body rotation on a viscous timescale $E^{-1}\Omega^{-1}$; see for example Spence, Foster & Davies (1992). When discussing stratified spin-up problems care must be taken concerning the definition of a spin-up time. Since the readjustment is localized and thus position dependent, it is possible to achieve a flow that matches the new conditions very quickly in some regions of the container (notably adjacent to the horizontal boundaries). Nevertheless, on defining the (global) spin-up time to be that at which the bulk of the fluid has adjusted to the new conditions, we conclude that the time taken for a stratified fluid to spin-up is $O(E^{-1/2})$ longer than for the equivalent homogeneous problem.

Buzyna & Veronis (1971) performed a sequence of careful experiments on the small-amplitude motion of a rotating stratified fluid. The experimental data (for a right circular cylinder filled with a linearly stratified fluid) were compared with the theoretical predictions of Holton (1965), Walin (1969), and Sakurai (1969). Although the boundary conditions applied by Holton were inappropriate for the experimental configuration used by Buzyna & Veronis, a comparison was still made since, in Holton's paper, some experimental work had been presented that compared favourably with the quantitative predictions of the analysis. The results of the experimental work of Buzyna & Veronis showed that the predictions of Walin and Sakurai were in agreement with the experimental data when considering the mid-plane of the contained flow. There were discrepancies between the predictions of Holton and the experimental data everywhere in the flow, but the theory of Walin and Sakurai only had small quantitative differences near the Ekman layer (especially near the corner region). The former inaccuracies can obviously be attributed to the incorrect treatment of the vertical wall-layer by Holton (casting some doubt on his experimental data), whereas for the latter disagreement, Buzyna & Veronis suggested that the difference may be attributed to nonlinear effects.

The linear, stably stratified spin-up problem for a circular cylinder is obviously rather specialized. In particular, it is unclear how the effects of density stratification, nonlinearity, background rotation and a more general container geometry will interact. One would intuitively expect that the introduction of boundaries that are neither perpendicular nor parallel to the vertical axis will establish a flow in which the effects of buoyancy are coupled into the usual Ekman boundary layer. Until recently very little work has been presented concerning buoyancy-affected Ekman layers, see for

example Garrett, MacCready & Rhines (1993), MacCready & Rhines (1991) and Duck, Foster & Hewitt (1997, referred to hereafter as DFH).

In this paper we wish to return to the boundary-layer problem formulated by DFH. Rather than discussing the global spin-up process, we shall present the results of an experimental investigation into the boundary layer that forms on the sloping wall of a conical container immediately after a change in rotation rate; the initial state of the fluid approximates a rigid-body rotation in all cases. The motivation for these experiments is to make a detailed comparison with the theoretical analysis of the boundary-layer evolution.

In §2 we review the formulation and conclusions of the theoretical predictions, based on the Boussinesq boundary-layer equations, from the point of view of the laboratory investigation. In §3 we discuss the experimental set-up and, in §4, make quantitative comparisons with the results of DFH over a wide range of parameters.

A detailed study of the complete set of steady solutions to the governing boundary-layer equations is beyond the scope of this paper. However, as for the swirling flow above a rotating disk, we note that a large number of steady states can be located at general parameter values. The stability of those states relevant to the experimental parameter regime is briefly considered in §5. A complete map of the spin-up/down parameter space is presented for a Schmidt number of 700, which is the appropriate value for the saline solution utilized in our laboratory experiments.

The stability results of §5, show that the eigenvalue spectrum has discrete and continuous components. In Appendix A we give some analytical results that suggest the continuous spectrum is always stable for regions of the parameter space relevant to the experimental work.

Finally, in Appendix B we present a brief outline of some numerical solutions (at large Schmidt number) to the unsteady boundary-layer equations that reveal a region of the parameter space within which a new form of finite-time breakdown can be observed. This type of evolution was not discovered in the previous analysis presented by DFH. Although the parameter values at which this new evolution can be found are not achievable in any global sense with our experimental apparatus, they are relevant to a more general boundary-layer problem and complete the previous description of DFH. The presence of the continuous spectrum in the linear stability analysis (as discussed in Appendix A) is crucial to the breakdown.

2. The boundary-layer analysis

The geometry under consideration is a conical container with associated angle α (in our experiments $\alpha = \pi/4$ as shown in figure 2) and an axis of rotation that is vertical. The density field of the fluid within the container is decomposed into a constant reference density, ρ_o, a 'linear'† stratification, $\bar{\rho}(z)$, and a general unsteady, axisymmetric component ρ' (here z is a vertical coordinate). In a spherical polar coordinate system (r^*, θ^*, ϕ^*) centred at the cone's apex, the full density field is $\rho(r^*, \theta^*, t) = \rho_o + \bar{\rho}(r^* \cos \theta^*) + \rho'(r^*, \theta^*, t)$, where t denotes time and $\rho', \bar{\rho} \ll \rho_o$.

The velocity components within the boundary layer, length and time are made dimensionless with respect to Ωh, h and Ω^{-1} respectively, and a non-dimensional buoyancy term is introduced $B = g\rho'/(\rho_o \Omega^2 h)$. Ω and h are characteristic rotation rate and lengthscale respectively, which in our experimental investigation are taken

---

† Curvature of the isopycnals caused by the rotation is discussed in §3.3.

to be the final angular frequency of the container and the distance between the axis and the container wall at the level that data are gathered (see figure 3).

A similarity-type solution is available, which removes the radial dependence in a manner analogous to the von Kármán solution for a swirling flow above a rotating disk. The similarity solution is only valid in a region sufficiently far away from the apex of the container; in fact it is required that $\hat{r} \gg E^{1/2}$, where $\hat{r}$ is a non-dimensionalized ($\hat{r} = r/h$) radial coordinate centred at the apex (we shall assume $E \ll 1$ throughout this work).

The initial state of the system is assumed to be a rigid-body rotation and the boundary-layer analysis of DFH describes the flow dynamics in an infinite geometry subsequent to an impulsive, nonlinear change in the rotation rate. The analysis of DFH applies to axisymmetric similarity-type solutions to the unsteady, nonlinear, Boussinesq boundary-layer equations. These solutions were classified according to their large-time behaviour over an unrestricted parameter range, the only exception being that the far-field fluid and container are not permitted to counter-rotate. This is not a conceptual restriction however.

Parameters of interest for this system are the Burger number, rotation ratio, cone angle and Schmidt number

$$S = N^2/\Omega_f^2, \quad \hat{W}_e = \Omega_i/\Omega_f, \quad \alpha, \quad \sigma = \nu/\kappa. \tag{2.1}$$

Here

$$N^2 = -\frac{g}{\rho_0}\frac{\mathrm{d}\bar{\rho}}{\mathrm{d}z}, \tag{2.2}$$

Ω_i, Ω_f are the initial/final angular frequencies of the container, ν is the kinematic viscosity and κ is the density diffusion coefficient.

DFH showed that the evolution of the boundary-layer system is governed by just two parameters (for a fixed Schmidt number σ), namely S^* and $\hat{W}_e$. This reduction in the number of parameters was achieved by absorbing the pressure, and cone-angle dependences into redefined versions of the Burger number, S (as defined above), and the buoyancy term B. This redefinition leads to the introduction of a 'modified Burger number', S^*, defined by

$$S^* = \hat{W}_e^2 + \sin\alpha(S\sin\alpha - \hat{B}_e). \tag{2.3}$$

The analysis of DFH allows for a density perturbation in the interior, which requires that the buoyancy is of the form $B = \hat{r}\hat{B}_e$ in this region. However, for application of the analysis to our experimental results we shall assume throughout that $\hat{B}_e = 0$ and that the interior stratification is that measured when the container was initially filled and at rest.

The final conclusions of the boundary-layer analysis are reproduced in figure 1, which shows the parameter space diagram for a Schmidt number of unity ($\sigma = 1$). As can be observed from the figure, there are four main regions corresponding to the four classifications of large-time behaviour, as follows.

Steady State. Following a positive change in the rotation rate of the container ($0 < \hat{W}_e < 1$), the boundary layer approaches a steady state when S^* is less than some critical value ($S^*_{crit}(\hat{W}_e)$). We must note that the geometry considered in the theoretical analysis is an *infinite* cone, and is therefore capable of maintaining a steady boundary-layer state with an associated mass transport up/down the inside of the container wall. In a finite container, mass transported in the boundary layers must eventually recirculate and lead to an adjustment to the interior conditions. Therefore, in our
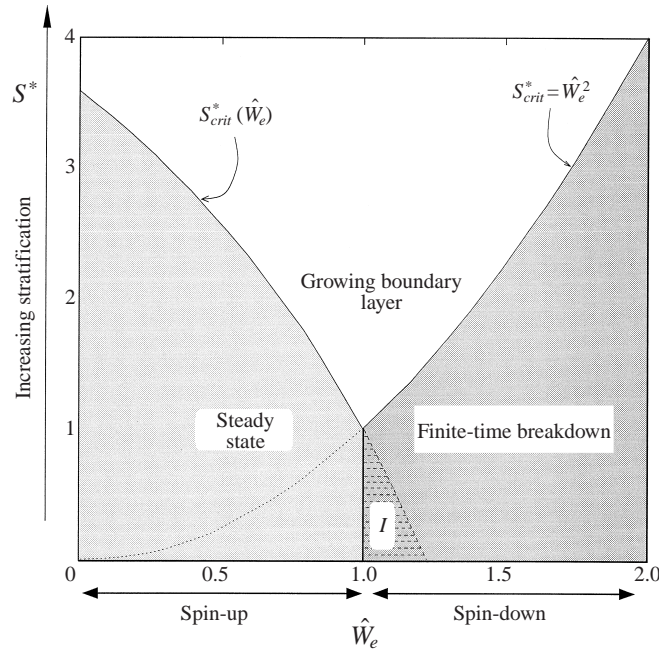
FIGURE 1. Parameter space for a Schmidt number of $\sigma = 1$. S^* is a measure of the importance of stratification, and $\hat{W}_e$ is the ratio of initial to final rotation rates. The evolution of the boundary layer has been classified according to its large-time behaviour.

laboratory experiments we may only see a boundary-layer state that approximates the appropriate steady state over a timescale for which recirculation effects are not important.

Growing boundary layer. In this regime a slowly thickening layer is obtained rather than the boundary layer attaining a steady state. A large-time asymptotic analysis of this regime shows that the velocity components in the boundary layer approach a limiting form, but only with a non-dimensional boundary coordinate that is scaled with $\hat{t}^{1/2}$, where $\hat{t}$ is a non-dimensional time ($\hat{t} = \Omega t$). In this case the boundary layer thickens into the interior and the mass transport in the layer (up/down the inside of the container walls) decays algebraically. This scenario is always predicted by the theoretical analysis for flows dominated by stratification effects ($S^* \gg 1$), and is associated with an inhibition of vertical mass transport by buoyancy forces.

Finite-time breakdown. The velocity components in the boundary layer become singular at a finite time. Unsteady numerical computations have been shown to agree with asymptotic descriptions of the singularity in this region.

Region 1. In this sub-region there are stable, steady states available, but these are not obtained by a time-dependent process from an initial state of rigid-body rotation. An evolution to a finite-time breakdown is preferred at these parameter values.

We must note that the results of figure 1 are presented for a Schmidt number of unity. Our laboratory experiments are performed with a saline solution for which the Schmidt number is $\sigma \approx 700$. A complete picture of the parameter space for large values of the Schmidt number is given in §5; however, for the subsequent experimental discussion it is enough, at this stage, to note that increasing σ has the effect of decreasing S^*_{crit}.

2.1. *Physical interpretation of the parameter space diagram*

There are a number of qualitative conclusions that may be drawn from the form of the parameter space diagram shown in figure 1 that will be useful in discussing the following experimental results.

The boundaries between evolution types are all known explicitly: $S^* = \hat{W}_e^2$ and $S^* = S_{crit}^*(\hat{W}_e)$. (In fact S_{crit}^* is determined by solving a reduced problem and represents a boundary in parameter space beyond which the primary steady state cannot be continued.) Consequently, it may be expected that the eventual behaviour of the solutions is largely insensitive to the initial conditions. In particular any form of rotation change (not necessarily impulsive) that is over a timescale less than the rotation period $(2\pi/\Omega_f)$ may not affect the classification of the large-time behaviour; this is easily shown to be the case for computational solutions of the unsteady boundary-layer equations.

Since it is only the buoyancy/acceleration due to gravity that defines the vertical direction, we can see that for the boundary layer, setting $\alpha = 0$ is equivalent to considering a homogeneous fluid. Although the main body of fluid can still have a density stratification, when $\alpha = 0$ the buoyancy coupling in the boundary layer is absent. In these cases the boundary layer is effectively the classical Ekman layer above an infinite rotating disk. The governing equations for the swirling flow above an infinite plane are thus recovered along a cross-section of the parameter space defined by $S^* = \hat{W}_e^2$; see for example Bodonyi (1978), Bodonyi & Stewartson (1977), Zandbergen & Dijkstra (1987) for details of the rotating-disk problem.

In figure 1, increasing S^* above S_{crit}^* and $\hat{W}_e^2$ corresponds to moving further into the growing boundary-layer region of the parameter space. The effect of an increased S^* (by considering a density stratification with a larger Brunt–Väisälä frequency for example) is, in general, to cause a more rapid growth (up to some limiting description) of the boundary layer into the interior. Likewise parameter values just below the S_{crit}^* boundary only attain a steady state after a considerable period of time, and the final steady state has a (large) boundary-layer thickness that also scales with the proximity of S^* to S_{crit}^* (see DFH). Therefore, in this sense, the change in the large-time evolution from a steady state to a growing boundary layer (as S^* becomes larger than S_{crit}^*) can be considered to be 'smooth', and it is unlikely that its location could be confirmed experimentally to any degree of accuracy.

As noted above, the parabola $S^* = \hat{W}_e^2$ corresponds to considering the equations governing the homogeneous swirling flow above an infinite rotating disk. In fact, in a typical laboratory experiment of the form we describe here, for a linearly stratified fluid in a conical container, the $S^* < \hat{W}_e^2$ region of parameter space corresponds to a statically unstable interior stratification. When considering a more general boundary layer however, we do not restrict the parameter space, but do recognize that it must be interpreted correctly when applied to a specific experimental investigation. Nevertheless, it must be noted that the finite-time breakdowns discussed by DFH for nonlinear spin-down ($\hat{W}_e > 1$) occur over relatively short timescales, typically within just a few background rotations even when the parameter values are only slightly within the breakdown region. It may therefore be possible for this mechanism to dominate in other flow configurations or in some local region of a laboratory experiment. However, as we shall discuss in §4.3, the relevance of the DFH boundary-layer analysis to the experimental spin-down readjustment process is open to question since the flow, in general, becomes non-axisymmetric in these cases.
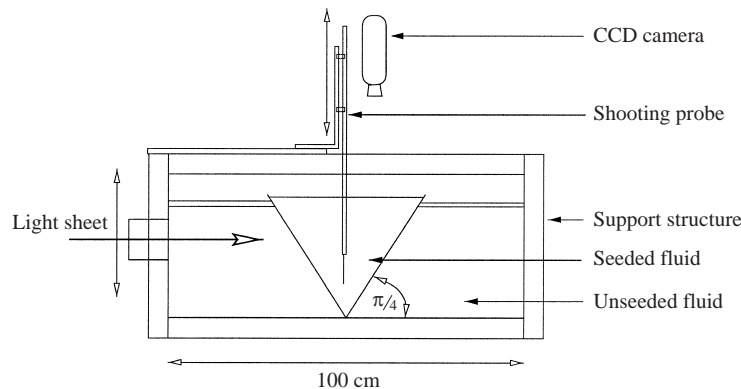
FIGURE 2. Experimental apparatus. The structure shown rotates on a levelled, computer-controlled turntable with the CCD camera fixed in the rotating frame.

3. Experimental configuration

A series of laboratory experiments have been performed to test the predictions of the boundary-layer analysis given by DFH. The apparatus used in the experimental investigation is shown schematically in figure 2. The fluid within the cone is seeded with particles of a mean diameter less than 250 microns, then the unsteady flow resulting from a change in the container rotation rate is visualized by illumination of these particles with a horizontal light sheet. A camera, fixed in the frame of the container, views the particle motion from above (figure 3). There can be significant changes in the uniformity of the light sheet intensity over a cross-section (figure 3) of the conical container, which can make resolution of particles by the tracking software (Dalziel 1992) difficult. These difficulties can be overcome by using diametrically positioned light sources to produce intersecting light sheets; however for the axisymmetric flow evolution it was found to be sufficient to obtain tracking data in the quarter of the cone cross-section nearest to the light source. The larger volume of unseeded fluid shown in figure 2 is used to reduce the optical difficulties associated with maintaining a horizontal light sheet through the container.

Density information is gathered with a calibrated aspirating conductivity probe, as described by Davies *et al.* (1991), which measures vertical density profiles near to the axis of rotation. In some experiments the profile was monitored at intervals throughout the readjustment phase and therefore measurements were restricted to the near-axis region. The experiments involve nonlinear changes in the container rotation rate and the density profiles were therefore taken near the centre of rotation (the area of least fluid velocity) to minimize any artificially introduced disturbances caused by flow around the probe shaft.

Typical laboratory parameter values used in this investigation are

light sheet radius	$0.08 \leqslant h \leqslant 0.11 \, \mathrm{m}$,
kinematic viscosity	$\nu \approx 10^{-6} \, \mathrm{m^2 \, s^{-1}}$,
Brunt–Väisälä frequency	$0 \leqslant N^2 \leqslant 5 \, \mathrm{s^{-2}}$,
Schmidt number	$\sigma = 700$,
typical angular frequency	$\pi/10 \leqslant \Omega \leqslant \pi/4 \, \mathrm{rad \, s^{-1}}$,
cone angle	$\alpha = \pi/4$.

The experiments are performed with a stable, (approximately) linearly stratified fluid, that has a density variation within the limits $\rho \in [1000, 1080] \, (\mathrm{kg \, m^{-3}})$. This density
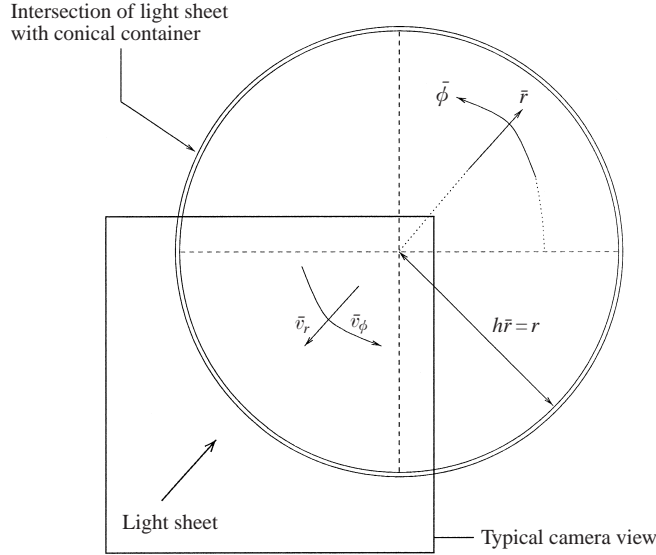
FIGURE 3. The laboratory coordinate system; $\bar{r} = r/h$ is a radial coordinate, non-dimensionalized with the light sheet radius h, and $\{\bar{v}_\phi, \bar{v}_r\}$ are non-dimensionalized velocity components. The dimensional fluid velocity is given by $\{v_\phi, v_r\} = h\Delta\Omega\{\bar{v}_\phi, \bar{v}_r\}$. For a swirl flow, the local angular frequency in the cross-section plane is denoted by $\omega = v_\phi/r$ and a non-dimensional quantity of interest is $|\omega/\Delta\Omega|$.

range is required to obtain the Brunt–Väisälä frequencies noted above. The height of the free surface above the apex of the container (measured while the container is at rest) was maintained at a constant 16.5 ± 0.2 cm throughout the experiments.

A typical Ekman number is $E \approx 10^{-4}$, for which we expect stratified (global) spin-up on a dimensional timescale $(E^{-1}\Omega^{-1})$ measured in hours rather than the several minutes necessary to achieve a readjusted state with a homogeneous fluid. We shall use the specific notation Ω_i and Ω_f when referring to the initial and final rotation rates of the container.

Because the container has a cross-section that varies with height, it is not possible to use the standard double reservoir (Oster 1965) technique for generating the linear density gradient. Similarly, filling the container with several distinct layers and waiting for a diffusion to an approximately linear stratification, in general, leads to large regions of low-N near the free surface and apex. Accurate (throughout the majority of the container depth) linear gradients were generated using a variation of the Oster method that involved the construction of a partitioned filling apparatus that compensated for the non-vertical sidewalls of the conical container.

3.1. *Homogeneous reference experiments*

In figures 4(a) and 4(b) we present typical evolutions of the angular frequency distribution for the spin-up of a homogeneous fluid in the conical container. The fluid density was chosen so that the particles experienced very little buoyancy force in order to maximize the suspension time and thus allow the residual motions in the container to decay to sufficiently low levels. The particles were tracked over a quarter of the cone, as indicated in figure 3, then averaged spatially and over a 2 s tracking interval. The raw data are then used to produce a segmented average over an interval $\bar{r} \in [i\delta, (i+1)\delta]$, where $\delta = 0.01$, for $i = 40, 41, \ldots, 99$. The smooth curve is simply a
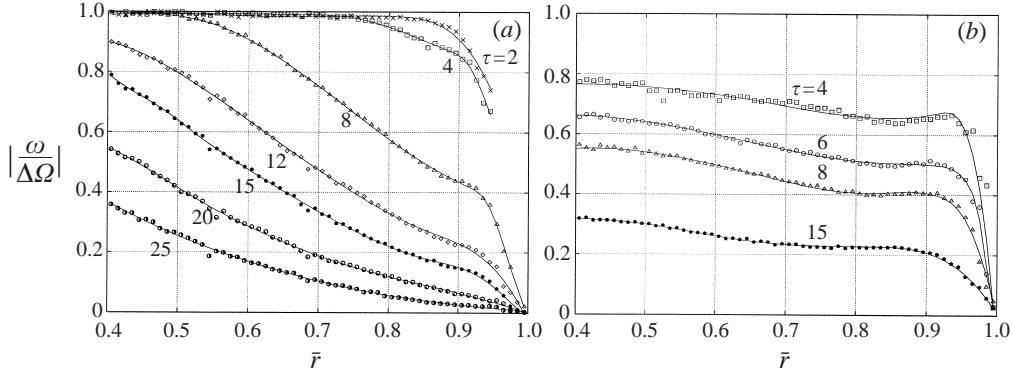
FIGURE 4. Homogeneous results, showing the development of $|\omega/\Delta\Omega|$, where ω is a local angular frequency (see figure 3) and $\Delta\Omega = |\Omega_i - \Omega_f|$. $\bar{r}$ is a dimensionless radial coordinate, where $\bar{r} = 0$ at the axis, $\bar{r} = 1$ at the container wall, and $\tau = \Omega_f t/2\pi$ is a rotation number. (a) Spin-up from $\Omega_i = 0\,\text{s}^{-1}$ to $\Omega_f = \pi/5\,\text{s}^{-1}$, (b) spin-down from $\Omega_i = \pi/5\,\text{s}^{-1}$ to $\Omega_f = \pi/10\,\text{s}^{-1}$, with a linear deceleration over the interval $\tau \in [0, 3]$.

b-spline fit to the data. The parameter τ shown in the figures can be thought of as a background rotation number, defined by $\tau = \Omega_f t/2\pi$. The initial state of rigid-body rotation corresponds to $\omega/|\Delta\Omega| = 1$, and the final state of rigid-body rotation is such that $\omega/|\Delta\Omega| = 0$.

Although the results of figure 4(a) are presented for a 'near-impulsive' change in the rotation rate (typically the rotation rate changes over a period of $\tau \in [0, 0.1]$), the spin-down results of figure 4(b) are shown for a linear deceleration of the tank to a state of rest over the period $\tau \in [0, 3]$. A deceleration of the container over a shorter period results in the development of a dominating centrifugal instability (at the light sheet level that was chosen for this experiment), which makes tracking results unreliable since the motion is strongly three-dimensional in the boundary layer.

Similar results can be shown for a range of rotation rate changes, background rotation values and light sheet levels. Typical features that are found in the homogeneous case are the distinctive curvature of the profiles of local angular frequency, regions of slightly increased angular frequency near to the boundary (figure 4b), and quasi-steady profiles over a short period of time after the rotation change (figure 4a). All these features are well known for homogeneous spin-up and can be attributed to an 'Ekman transport' in the boundary layer, which results in a 'fast' spin-up over the dimensional timescale $E^{-1/2}\Omega^{-1}$ through a meridional circulation (see for example, Benton & Clark 1974).

3.2. *Evolution of the density profile*

Each time the container is filled with an appropriately stratified fluid, a typical sequence of experiments is:

$$
\begin{array}{llll}
(a) & \text{spin-up,} & \Omega_i = 0\,\text{s}^{-1}, & \Omega_f = \pi/5\,\text{s}^{-1}, \\
(b) & \text{spin-up,} & \Omega_i = \pi/5\,\text{s}^{-1}, & \Omega_f = \pi/4\,\text{s}^{-1}, \\
(c) & \text{spin-down,} & \Omega_i = \pi/4\,\text{s}^{-1}, & \Omega_f = \pi/5\,\text{s}^{-1}, \\
(d) & \text{spin-down,} & \Omega_i = \pi/5\,\text{s}^{-1}, & \Omega_f = \pi/10\,\text{s}^{-1}, \\
(e) & \text{spin-up,} & \Omega_i = \pi/10\,\text{s}^{-1}, & \Omega_f = \pi/5\,\text{s}^{-1}, \\
(f) & \text{spin-down,} & \Omega_i = \pi/5\,\text{s}^{-1}, & \Omega_f = 0\,\text{s}^{-1}.
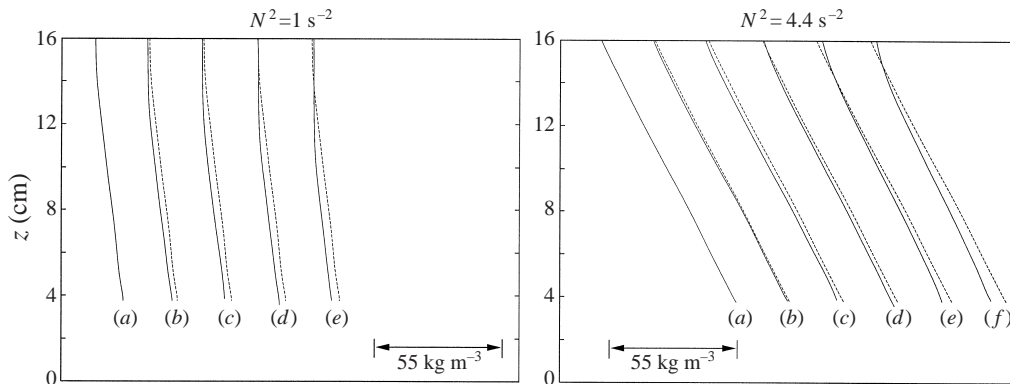\end{array}
$$

FIGURE 5. Evolution of the density profile: a sequence of vertical density profiles; the stated Brunt–Väisälä frequency denotes a local value measured at the level of the light sheet when the container is at rest. The initial profile is repeated at each stage as the dashed line, a description of the labels (*a*)–(*f*) is given in the text.

Density profiles are taken before each change in rotation rate, and at intervals during some of the experiments. A significant period is required for the readjustment to take place between each change. A comparison of profile measurements is given in figure 5. The labels (*a*)–(*f*) denote profiles taken immediately *before* the corresponding change denoted in the list above. The data presented in the figure are running averages of those gathered from the aspirating conductivity probe, and the original profile (*a*) is given at each stage for comparison.

Although great care was taken in the experiments to ensure that the aspirating probe remained free of blockages, it is possible for the quantitative data to vary by small amounts if particles are drawn into the probe tip. However, the qualitative features of figure 5, namely the development of a low-N region near the surface and a slight downward shift in the profile at high rotation rates are repeatable.

For stratification at a sufficiently 'low' Brunt–Väisälä frequency (e.g. $N^2 \leqslant 1\,\mathrm{s}^{-2}$ for rotation rates typical in these experiments), completion of the sequence (*a*)–(*f*) above can be difficult to justify since centrifugal instabilities associated with the nonlinear spin-down process can cause significant mixing near the free surface. Obviously, any transient centrifugal instability will develop in the boundary-layer region during spin-down, and the larger radius of the container near the free surface means that supercritical conditions are maintained there over a longer period of time than elsewhere. The transient growth of Taylor–Görtler vortices and the associated vertical motion is therefore suggested as the mechanism responsible for the development of the low-N region near the surface on this timescale. The readjustment process for spin-down cases will be discussed in more detail in §4.3.

3.3. *Experimental error*

3.3.1. *Particle tracking*

Quantitative data are obtained by tracking the particles over a quarter view of the cone (as shown in figure 3) then averaging spatially over the tracking domain (when the flow is axisymmetric) and temporally over a period between 0.5 to 2 s depending on the experiment. We have given, where appropriate, some graphical indication of the scatter in the data obtained in this manner.

It is possible for particles to adhere to the inner surface of the cone, resulting in a bright annular region when illuminated by the light sheet. Because the light sheet is approximately 6 mm deep where it intersects with the container, this bright region can make particle tracking difficult immediately adjacent to the wall.

For large changes in rotation rate the fluid velocity of the resulting motion relative to the container can be sufficient for the particles to move significantly in the 1/50th of a second between consecutive interlace fields of the video. When combining these fields for tracking this can result in 'ghost' particles, that is, single particles being effectively in two positions. To avoid these complications the particle size (as seen in the video recordings) was maximized by adjusting the brightness level and defocusing (very slightly) the CCD camera. The interlace fields were averaged where problems were unavoidable; however, this was only required for highly nonlinear changes in the rotation; this latter option obviously reduces the tracking resolution.

3.3.2. *Free-surface curvature*

We are considering a density-stratified fluid that is initially either at rest or rotating at a constant angular frequency Ω_i. All the results obtained from the laboratory investigations discussed in this paper have been obtained for a fluid-filled conical container with a free surface. This configuration will obviously be affected by rotation, leading to curvature of the free surface and a deviation from the density profile as measured whilst the container is at rest. (The introduction of a rigid lid would reduce the free-surface curvature effects but at the expense of introducing a further boundary layer, the influence of which may dominate in some regions of the flow.) However, since the maximum initial angular frequency considered in this work is $\pi/4\,\mathrm{s}^{-1}$, the associated Froude number based on the maximum radius of the container and maximum depth of fluid is $F \approx 0.05$. Therefore the parabolic curvature of the free surface is small relative to the fluid depth.

The parabolic curvature of the isopycnals also causes a refractive index gradient that will inevitably cause some deviation of the light sheet from the horizontal; however this difference is less than the width of the sheet over the region of interest. The modified Burger number, S^*, depends on the Brunt–Väisälä frequency, N, for which we use a local value at the light sheet level, as measured while the container is at rest. There can be some slight adjustment to the exact value of N caused by the rotation effects, but at such small rotation rates this effect is neglected.

3.3.3. *Other sources of error*

In none of the results have we allowed for the variation of the kinematic viscosity possible at high salinity levels, which can be as much as 10% for the working fluids in our experiments.

The length scale used in the non-dimensionalization process is the radius of the light sheet (or equivalently, since the coneangle was fixed at $\alpha = \pi/4$, the vertical apex to light sheet distance). This light sheet level is determined by using the aspirating probe (whose position is known to ± 1 mm) to measure the z-location of the top and bottom of the light sheet and then averaging the two values. As noted above, at the centre of the conical container the light sheet is approximately 6 mm deep since some divergence is unavoidable.

The initial and final angular frequencies of the container were accurate to $\pm 0.002\,\mathrm{rad\,s}^{-1}$; however there was some decaying oscillation of the rotation rate subsequent to large, nonlinear, changes in the rotation rate. This oscillatory behaviour is a property of the drive mechanism and has been confirmed by tracking

an arrangement of reference lights on the rotating table with the camera in the non-rotating frame. The oscillations are only noticeable for large $|\Delta\Omega|$ and decay within a few rotations of the table with no significant effect on the large-time behaviour of the fluid system.

In particle tracking tests performed some 24 hours after a rotation rate change (with a linearly stratified fluid) there was some evidence of a mean drift relative to the container; the velocities involved were an order of magnitude smaller than typically measured in an experiment. The effect of this drift of particles is not believed to be significant and is related to the Sweet–Eddington circulation; see Buzyna & Veronis (1971). The circulation can be a significant factor at large rotation rates, but the effect is small in the experiments we consider here. The deviation from a rigid-body rotation is difficult to observe at our parameter values without digitally processing the video recordings of the particles to produce particle streaks on a timescale comparable with several rotations of the tank.

It is difficult to provide error estimates for the axial symmetry of the container. No evidence of any divergence from an axisymmetric flow on a dimensional $E^{-1/2}\Omega_f^{-1}$ timescale was observed in the homogeneous spin-up experiments or on any larger timescale for the stratified spin-up experiments.

4. Comparison of the boundary-layer theory with laboratory experiments

It is possible to make some detailed comparisons between the particle tracking data obtained from spin-up experiments and the predictions of the boundary-layer analysis. However, the coordinate system and non-dimensionalization utilized in the theoretical approach need some consideration before a direct comparison can be made.

DFH used a spherical-polar coordinate system (r^*, θ^*, ϕ^*) to describe the flow. The coordinate system is centred on the apex of the conical container, with $(v_r^*, v_\theta^*, v_\phi^*)$ denoting the radial, meridional and azimuthal velocity components respectively. The boundary layer on the inside of the conical surface is defined through the scaled normal coordinate $\theta \in [0, -\infty)$, where

$$\theta^* - (\pi/2 - \alpha) = E^{1/2}\theta. \tag{4.1}$$

Here $E = v/(\Omega h^2)$ denotes the Ekman number based on a typical lengthscale, h, angular frequency Ω and kinematic viscosity v.

An axisymmetric, non-dimensional, solution of similarity-type, was sought for the governing Boussinesq boundary-layer equations:

$$\hat{r} = r^*/h, \tag{4.2}$$

$$\Theta = \hat{r}\theta = O(1), \tag{4.3}$$

$$\hat{v}_r = \hat{r}\hat{U}(\Theta, \hat{t}) + \ldots, \tag{4.4}$$

$$\hat{v}_\theta = \hat{V}(\Theta, \hat{t}) - \Theta\hat{U}(\Theta, \hat{t}) + \ldots, \tag{4.5}$$

$$\hat{v}_\phi = \hat{r}\hat{W}(\Theta, \hat{t}) + \ldots, \tag{4.6}$$

$$\hat{t} = \Omega t, \tag{4.7}$$

where $\hat{r} \gg E^{1/2}$. To avoid confusion with the previous definitions of the experimental work, the hat-notation has been introduced to indicate quantities that have been non-dimensionalized as described by DFH.
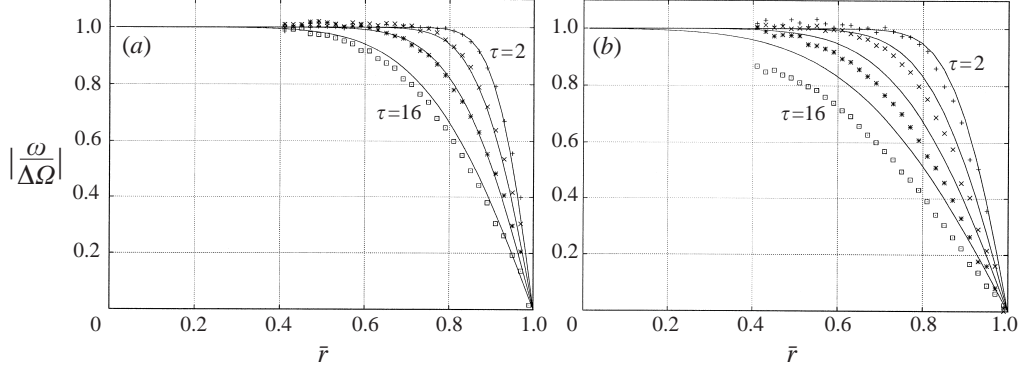
FIGURE 6. A comparison between experiment (data points) and boundary-layer analysis predictions (solid lines) at $\tau = 2, 4, 8, 16$ ($\tau = \Omega_f t/2\pi$), showing the development of $|\omega/\Delta\Omega|$, where ω is a local angular frequency (see figure 3), and $\Delta\Omega = |\Omega_i - \Omega_f|$, $\Omega_i = 0\,\mathrm{s}^{-1}$, $\Omega_f = \pi/5\,\mathrm{s}^{-1}$. (a) $N^2 = 2.5\,\mathrm{s}^{-2}$ ($\hat{W}_e = 0$, $S^* = 6.3$), (b) $N^2 = 4.4\,\mathrm{s}^{-2}$ ($\hat{W}_e = 0$, $S^* = 11.2$). Numerical results are obtained with $\sigma = 700$.

The equations considered by DFH were non-dimensionalized so that the azimuthal velocity component in the boundary layer is unity at the container wall, $\hat{W}(\Theta = 0, \hat{t} > 0) = 1$. Since a spherical-polar coordinate system was chosen, this non-dimensionalization needs to be related to that utilized in a typical laboratory experiment. If, from a non-rotating frame of reference, the container is rotating with angular frequency Ω_i at $\hat{t} = 0-$, with an impulsive change to Ω_f at $\hat{t} = 0$, then the dimensional azimuthal velocity at the cone is $v_\phi^*(r^*, \theta^* = \pi/2 - \alpha, t > 0) = r^* \Omega_f \cos\alpha$. The $\cos\alpha$ coefficient is introduced because r^* is a radial coordinate in a *spherical* rather than cylindrical coordinate system. Thus, in effect, the rotation rate used in the non-dimensionalization process of DFH is $\Omega = \Omega_f \cos\alpha$.

To compare the results of the boundary-layer analysis with those of the particle-tracking experiments we can examine a normalized, non-dimensional angular frequency, $\bar{\omega}$ (relative to a rotating frame of reference fixed with the container) compared to a non-dimensional radial coordinate, $\bar{r}$, (relative to the axis of rotation) at non-dimensional times $\bar{t}$, where we define

$$\bar{\omega}(\bar{r}, \bar{t}) = |\omega/\Delta\Omega| = |\Omega_f(1 - \hat{W}(\Theta, \hat{t}))/(\Omega_f - \Omega_i)|, \tag{4.8}$$

$$\bar{r} = 1 - \bar{E}^{1/2}\Theta/\sin\alpha, \tag{4.9}$$

$$\bar{E} = \nu/(\Omega_f h^2 \cos\alpha), \tag{4.10}$$

$$\bar{t} = \hat{t}/\cos\alpha = \Omega_f t. \tag{4.11}$$

These definitions are consistent with those introduced in §3, as summarized by figure 3, and for comparisons with the experimental results we use $\alpha = \pi/4$.

4.1. *Comparison of local angular frequency*

In figures 6 and 7 we present some comparisons of the normalized, local angular frequency obtained from particle tracking (data points) with the corresponding prediction, $\bar{\omega}(\bar{r}, \bar{t})$, of the boundary-layer analysis (solid lines). The theoretical results are presented in the form (4.8)–(4.11) above, with the change in rotation rate assumed to be impulsive. The data points shown in the figure are a segmented average of the particle tracking data obtained over the quarter-cone viewed by the camera. The
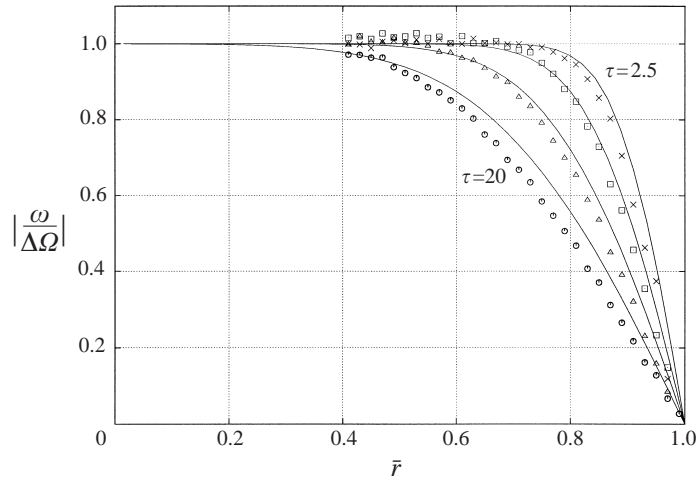
FIGURE 7. As figure 6 but at $\tau = 2.5, 5, 10, 20$, and $\Omega_i = \pi/5\,\text{s}^{-1}$, $\Omega_f = \pi/4\,\text{s}^{-1}$. $N^2 = 4.4\,\text{s}^{-2}$ ($\hat{W}_e = 4/5$, $S^* = 11.2 + \hat{W}_e^2$).

tracking interval over which the data are acquired is typically 1 or 2 s, depending on the speed of the flow and particle number density within the light sheet.

The two comparisons presented in figure 6 are for a spin-up from rest to a final angular frequency of $\pi/5\,\text{s}^{-1}$, corresponding to $\hat{W}_e = 0$ in the notation of DFH; obviously this flow is dominated by nonlinear effects. We note that, in the latter case (figure 6b), the agreement can be improved by assuming an adjustment of the kinematic viscosity (to account for the density change at high Brunt–Väisälä frequencies); this results in a larger Ekman number and a corresponding thickening of the theoretically predicted profiles. However, the boundary-layer analysis assumes a constant viscosity with respect to the vertical coordinate, and therefore, for consistency, we use the value $v = 10^{-6}\,\text{m}^2\,\text{s}^{-1}$, which is for water at room temperature with a density of approximately $1000\,\text{kg}\,\text{m}^{-3}$. In figure 7 we present a similar comparison at a more general point in the parameter space.

The comparisons shown in figure 6 and 7 are over a timescale comparable to that required for homogeneous spin-up and there is clearly a remarkable level of quantitative agreement. The theoretical predictions of DFH are made with a boundary-layer approximation, which, as can be seen from figures 6 and 7, is difficult to justify over any significantly larger timescale.

Although it is difficult to verify experimentally, the level of agreement between experiments (which gather data from a range of heights within the total fluid depth) and theory suggests that the similarity solutions introduced by DFH were realized throughout the majority of the container during spin-up. Obviously there must exist regions near to the free surface and apex of the cone within which there is some divergence from the similarity form. The region near the apex is over a lengthscale $hE^{1/2}$ as noted previously; however we have no such estimate of the corresponding region near to the free surface. As we shall discuss in later Sections, the effects of the finite geometry are eventually felt in many areas of the parameter space as Ekman mass transport in the boundary layers results in recirculation affecting the interior flow.
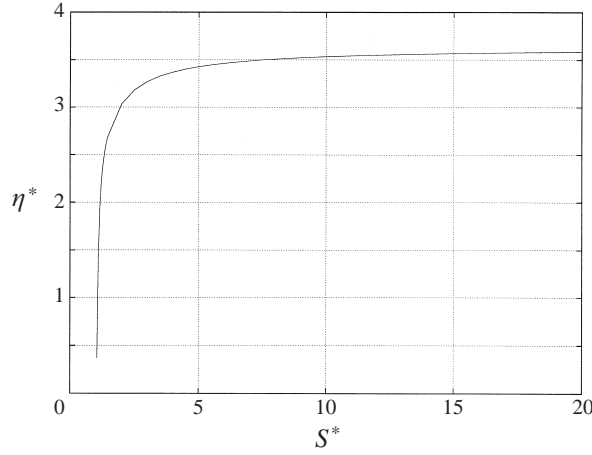
FIGURE 8. Variation of η^* with S^* as predicted by the large-time asymptotics of the boundary-layer analysis. Shown here for $\sigma = 700$, $\hat{W}_e = 0$.

4.1.1. *Estimate of the boundary-layer thickness*

It has been shown by DFH that the large-time behaviour of the growing boundary layer can be described asymptotically with an outer layer on the non-dimensional boundary-layer scale $\eta = \Theta/\hat{t}^{1/2} = O(1)$; the definitions of Θ and $\hat{t}$ are given in (4.3) and (4.7). Therefore, a dimensional 'thickness', of the boundary layer visualized by the light sheet is simply (for sufficiently large times) $\gamma = (v/\Omega)^{1/2}\eta^*\hat{t}^{1/2}$, where η^* is related to some arbitrary thickness measure (for example, where the local angular frequency is 99% of that in the interior). In the notation of the theoretical approach, a more useful expression (in this particular problem) is the ratio of the boundary-layer thickness to the light sheet radius, $\tilde{\gamma}$ say, which is (following the arguments at the start of this Section)

$$\tilde{\gamma} = \sqrt{2}E^{1/2}\eta^*\bar{t}^{1/2}, \tag{4.12}$$

where $E = v/\Omega_f h^2$, and h is the radius of the light sheet.

The functional dependence of η^* on the parameters S^*, $\hat{W}_e$ and σ is determined by the large-time asymptotics of the boundary-layer analysis. In figure 8 we show the dependence of η^* on the modified Burger number S^* for $\sigma = 700$ and $\hat{W}_e = 0$, which are typical laboratory parameters for the spin-up from rest of a salt-water solution. As suggested in the figure, η^* approaches zero as S^* approaches the critical value $S^*_{crit}(\hat{W}_e = 0; \sigma = 700)$. This must be the case since the system evolves to a steady state for $S^* < S^*_{crit}$ and the large-time analysis involving the temporally growing outer layer no longer holds. The data shown in figure 8 suggests that (at least when $\hat{W}_e = 0$, $\sigma = 700$) we should expect the rate at which the boundary layer grows into the interior to be only weakly dependent on S^* for modified Burger numbers above a limiting value.

An analysis of the large-time limit provides a good estimate for a typical spin-up problem; this can be argued more precisely with comparisons between the unsteady computations and the large-time asymptotic predictions, but we do not do so here. Given an estimate of the upper limit of $\tilde{\gamma}$, below which the boundary-layer approximation gives good quantitative results, we can use the large-time asymptotic result (4.12) to provide a similar approximation to the timescale on which accurate quantitative predictions can be expected over a range of S^*.
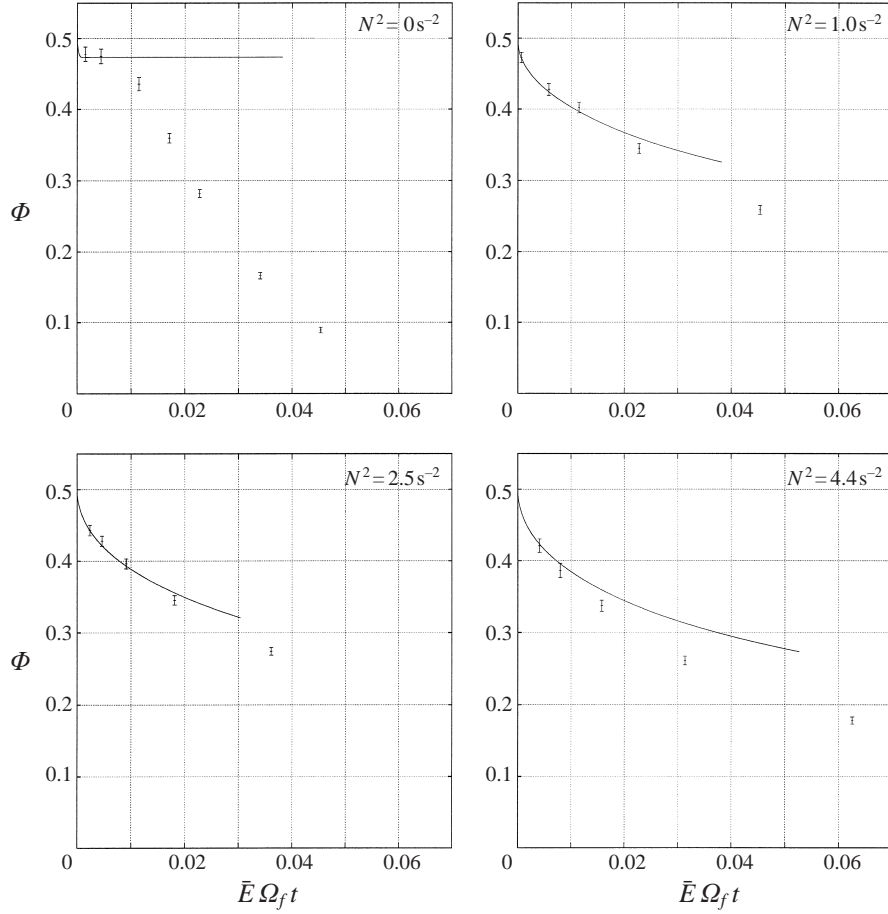
FIGURE 9. A comparison between experiment and boundary-layer analysis predictions. Parameter values are $\Omega_i = 0\,\mathrm{s}^{-1}$, $\Omega_f = \pi/5\,\mathrm{s}^{-1}$, and $N^2 = 0, 1, 2.5, 4.4\,\mathrm{s}^{-2}$, corresponding to $\hat{W}_e = 0$ and $S^* = 0, 2.5, 6.3, 11.2$ respectively. Numerical results are obtained with $\sigma = 700$. Note that data gathered at small values of $\bar{t}$ are not shown for clarity, but are discussed in §4.2.1.

4.2. *A global measure of the readjustment*

Another obvious way to compare the theoretical approach with experimental data is to examine how some global measure of the axisymmetric flow (at the level of the light sheet) varies with time. A dimensionless quantity that is easily obtained from the particle tracking data is

$$\bar{\Phi}(\bar{t}) = \left| \int_{\bar{r}=0}^{\bar{r}=1} \bar{v}_\phi(\bar{r}, \bar{t}) \, \mathrm{d}\bar{r} \right|, \quad \text{where } \bar{v}_\phi = \frac{v_\phi}{h|\Omega_i - \Omega_f|}, \tag{4.13}$$

which can be thought of as a mean flow component in the quarter-cone view, or a normalised measure of the azimuthal transport within the light sheet.

A comparison between theory and experiment for the quantity $\bar{\Phi}$ (averaged over the quarter-cone viewed by the camera) is given in figure 9; the time-axis has been non-dimensionalized and scaled with the Ekman number, $\bar{E}$, as defined in (4.10). The error bars shown in figure 9 represent a measure of the data scatter obtained from the particle tracking process. For an ideal impulsive change in the container rotation rate
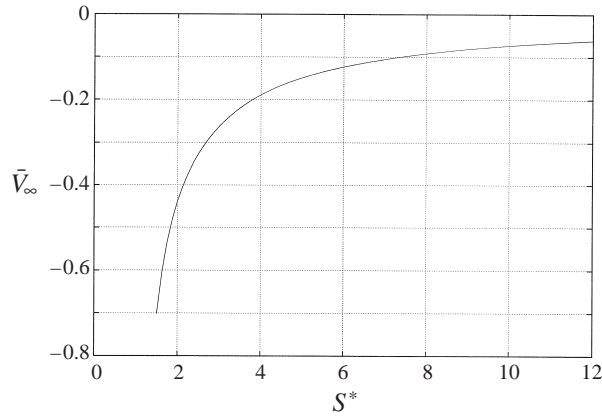
FIGURE 10. The qualitative effect of varying S^* (when $\hat{W}_e = 0$, $\sigma = 700$) on the Ekman transport in the growing boundary-layer scenario.

$\bar{v}_\phi/(h|\Omega_i - \Omega_f|) = \bar{r} + O(\bar{E}^{1/2})$, for $\bar{t} \ll 1$, and therefore $\bar{\Phi}(\bar{t} = 0+) = \frac{1}{2}$ for the theoretical results, as shown in the figure. Obviously, the experimental apparatus cannot be adjusted impulsively and has a small response time; therefore the experimental data points actually approach $\bar{\Phi} = 0$ at sufficiently small times rather than showing an impulsive change from $\bar{\Phi} = 0$ to $\bar{\Phi} = 1$ at $t = 0$; we shall discuss the $\bar{t} \ll 1$ regime in §4.2.1.

The agreement between theory and experiment (as shown in figure 9) remains when $\bar{\Phi} - 0.5$ is not too large (which corresponds to requiring that the boundary-layer approximation still holds). We can interpret the timescale of figure 9 by noting that, using the above estimate (4.12) with typical values of $\eta^* \approx 3.5$ (see figure 8) and $\tilde{\gamma} = \frac{1}{2}$ (a ratio of boundary-layer thickness to light sheet radius of $\frac{1}{2}$, cf. figures 6 and 7) gives a time of $\bar{E}\Omega_f\bar{t} \approx 1/7^2\sqrt{2} \approx 0.014$. Therefore, the eventual divergence of the experimental data from theoretically predicted values over the timescale shown in figure 9 (for $N^2 \geqslant 1$) is consistent with a failure of the boundary-layer approximation. It appears that the boundary-layer analysis overestimates the quantity $\bar{\Phi}$ beyond this timescale, which corresponds to a similar overestimation of the time necessary for readjustment to take place. Since we are primarily interested in making comparisons with the boundary-layer analysis, we do not give any detailed quantitative experimental data for the timescale required for a global spin-up. We note that the non-dimensional timescale shown in figure 9 equates to approximately 20 minutes based on a typical value of $\bar{E} = 10^{-4}$.

It is interesting to compare the decay of the quantity $\bar{\Phi}$ at low S^* with the data gathered at higher values, as shown in figure 9. As we have noted previously in §2.1, at sufficiently low values of S^* the analysis predicts that the boundary layer should attain a steady state rather than gradually thickening into the interior. In particular, a *steady* (von Kármán) solution is predicted for spin-up from rest in a homogeneous fluid, $N^2 = 0\,\mathrm{s}^{-2}$, since the appropriate point in parameter space ($S^* = \hat{W}_e = 0$) lies within the steady-state region for all values of the Schmidt number. It is evident from the $N^2 = 0\,\mathrm{s}^{-2}$ results of figure 9 that there is a sudden divergence of the experimental data from the predicted value of $\bar{\Phi}$ corresponding to the von Kármán state. To resolve this apparent discrepancy we obviously have to interpret the boundary-layer analysis in terms of the finite geometry of the container, the level of the light sheet, and the Ekman transport up/down the container wall. In particular, the difference between

the experimental data and theoretical predictions for a homogeneous fluid is caused by a sustained mass transport towards the free surface in the boundary layer (since there is no inhibition by buoyancy forces). This results in a global recirculation that acts to alter the interior flow conditions, leading to a rapid change in $\bar{\Phi}$.

Recirculation effects can also be obtained for stratified fluids, even at values of S^* for which steady states are not predicted. It has been shown by DFH that an asymptotic description of the evolution leading to a gradually thickening boundary layer can be given in the large-time limit. In particular DFH discuss the quantity $\hat{V}_\infty$, which is essentially a measure of the fluid velocity normal to the boundary at the boundary-layer edge. It was shown that

$$\hat{V}_\infty = \bar{V}_\infty \hat{t}^{-1/2} + \cdots, \qquad (4.14)$$

where $\hat{V}_\infty(\hat{t}) = \hat{V}(\Theta \to -\infty, \hat{t})$, as defined by (4.3), and $\bar{V}_\infty$ is a function of S^*, $\hat{W}_e$ and σ. In figure 10 we show how the leading-order quantity $\bar{V}_\infty$ varies with S^* at $\hat{W}_e = 0$ ($\sigma = 700$), as determined (numerically) from the large-time asymptotics; these values of σ and $\hat{W}_e$ correspond to a typical laboratory experiment for spin-up from rest, as shown in figure 9. Obviously, $\bar{V}_\infty$ is related, through the continuity of mass constraint, to the Ekman transport, and, as can be seen in the results of figure 10, the analysis predicts a significantly larger mass transport in the Ekman layer for $S^* \approx 2$ when compared to $S^* \approx 6, 11$.

Therefore, although in a growing boundary-layer evolution (as described in §2) the mass transport is predicted to decrease with the square-root of time, the decay for $S^* \approx 2$ (in our spin-up from rest, $\hat{W}_e = 0$, experiments) seems to be sufficiently slow for a slight meridional circulation to take place. This mechanism acts to decrease the overall spin-up time, causing relatively sudden changes in the gathered data as the recirculation affects the fluid at the level of the light sheet. A comparison of experimental data gathered for three different Brunt–Väisälä frequencies is shown in figure 11 at a non-dimensional time of $\bar{t} = 64\pi$ ($\tau = 32$). The data points of the figure are a segmented average of the raw tracking data, and the solid lines are simply a smooth fit to the data points. We can again note the distinctive curvature of the $N^2 = 1 \, \mathrm{s}^{-2}$ profile, indicating that some slight meridional circulation has occurred before the mass transport in the boundary layer can be inhibited by buoyancy effects.

We should note that the effect of varying S^* on the mass transport, as represented by $\bar{V}_\infty$ in figure 10, has been approximated by utilizing the large-time behaviour of the growing boundary-layer asymptotics of DFH. Unsteady computations for spin-up from rest ($\hat{W}_e = 0$) suggest that the leading-order asymptotic description of $\hat{V}_\infty = \bar{V}_\infty \hat{t}^{-1/2}$ is generally a good description within just two or three rotations of the system, although there can be a significant superimposed oscillation at the frequency $N \sin \alpha$.

The overall conclusions are that for $S^* < S^*_{crit}$, in which a steady Ekman transport is predicted, and for S^* 'slightly above' S^*_{crit}, in which a significant (relative to the container size/light-sheet level) transient Ekman transport takes place, we need to take account of the finite geometry in any description unless considering only the short-time behaviour. At a sufficiently large Brunt–Väisälä frequency however, the growing boundary-layer analysis of DFH provides an accurate quantitative description of the flow since any global recirculation is strongly inhibited by buoyancy effects.

4.2.1. *Short-time response of the container*

As noted in the first comment of §2.1 we expect that the large-time behaviour should be at least qualitatively comparable irrespective of the exact form of the
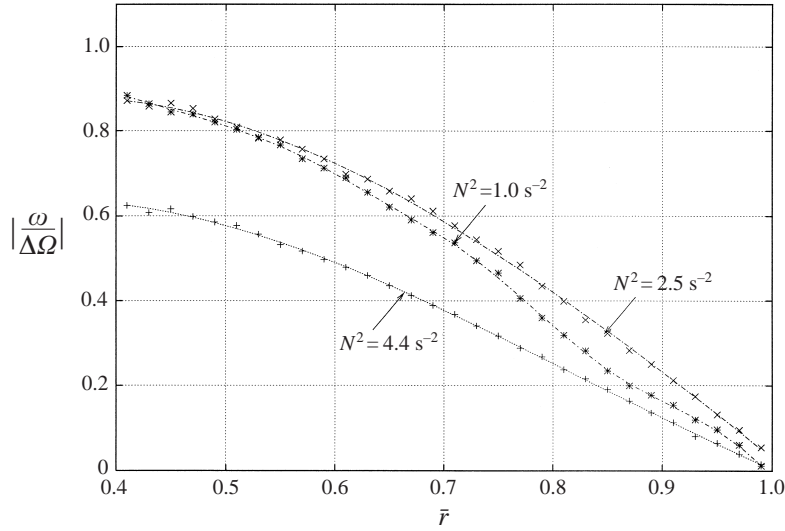
FIGURE 11. A comparison of experimental data gathered at Brunt–Väisälä frequencies corresponding to $N^2 = 1.0, 2.5, 4.4\,\mathrm{s}^{-2}$ ($S^* \approx 2.5, 6.3, 11.2$) at a fixed non-dimensional time of $\tau = 32$ for a spin-up $\Omega_i = 0\,\mathrm{s}^{-1}$, $\Omega_f = \pi/5\,\mathrm{s}^{-1}$.

rotation rate change. Nevertheless, for a system as shown in figure 2 the large inertia that has to be overcome to produce nonlinear changes in the rotation rate suggests that the short-time response should still be considered. Another motivation for examining the system within the first few rotations of the container is to compare the experimental and theoretical results, at low values of S^*, on a timescale for which the meridional circulation has little effect at the level visualized by the light sheet.

In figure 12 we present comparisons of the experimentally determined values of the quantity $\bar{\Phi}$ with the theoretically predicted values. A dimensional timescale has been used in the comparison, and we concentrate on the first 40 s after a rotation rate change to 6 r.p.m. from an initial state of rest, which corresponds to approximately the first four rotations of the container. The error bars shown in the figure are used to represent the data scatter obtained from the particle tracking process. The tracking data are obtained over a timescale of approximately 0.5 s; therefore, during the near-impulsive change in the rotation rate, the data scatter is more pronounced since the flow is evolving more rapidly. The difference between the experimental data and predicted values at small times ($t < 5\,\mathrm{s}$) is caused by assuming that the change in rotation is impulsive in the theoretical approach.

In the homogeneous case, $N^2 = 0\,\mathrm{s}^{-2}$, there is clearly some agreement between the steady von Kármán solution and the experiments on a timescale that is larger than the time taken for the container to attain its new rotation rate but still shorter than that required for recirculation effects to dominate at the light sheet level. It is also clear that in all cases there is some degree of decaying oscillation in the quantity $\bar{\Phi}$. As noted previously, the short oscillatory phase (lasting just a few rotations) is caused by non-uniform rotation of the apparatus after large nonlinear changes in the angular frequency. The oscillations shown in figure 12(*b*) represent a worst case, with an acceleration of the experimental apparatus from rest to 6 r.p.m. over a period of approximately 3 s. There is little evidence of this transient phase affecting the later dynamics of the fluid.
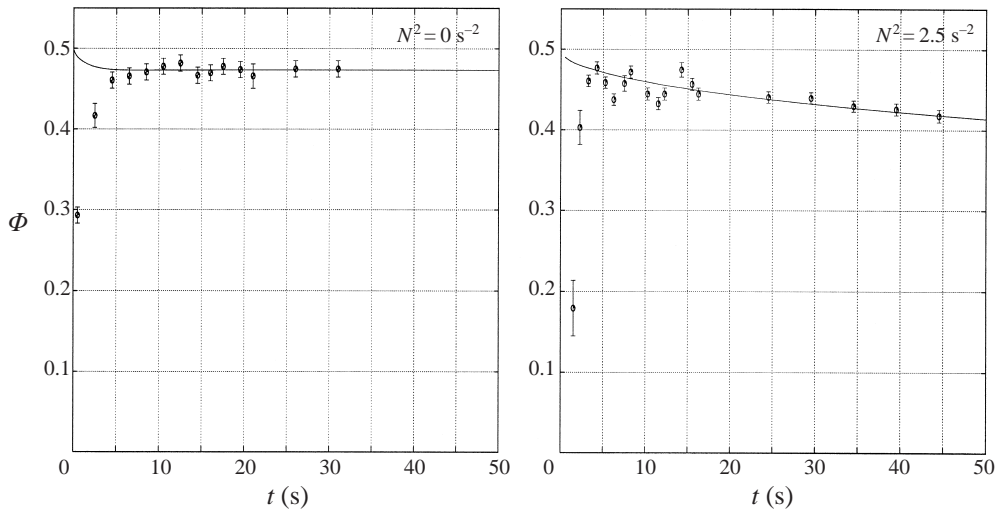
FIGURE 12. Short-time response to the near-impulsive change in rotation rate. $\Omega_i = 0\,\text{s}^{-1}$, $\Omega_f = \pi/5\,\text{s}^{-1}$. The solid line shows the predictions of the boundary-layer analysis with an impulsive change in the rotation rate. Numerical results are obtained with $\sigma = 700$.

4.3. *Spin-down, $\hat{W}_e > 1$*

The results presented above only show cases in which the rotation rate of the container has been increased, corresponding to $0 < \hat{W}_e < 1$. We must note that the axisymmetric boundary-layer analysis, although very successful in the spin-up cases, does not provide even qualitative agreement (in general) with the experiments for $\hat{W}_e > 1$.

For moderate values of $\hat{W}_e > 1$ it is possible to obtain results that can be matched to the growing boundary layer scenario (especially for cases where the effects of a stable stratification dominate). Nevertheless, for a general, nonlinear, spin-down experiment, the flow evolves through a transient stage dominated by a centrifugal instability (i.e. a Taylor–Görtler (T–G) instability) and then, settles down to a non-axisymmetric flow. This eventual non-axisymmetric behaviour in the decelerating flow is experimentally repeatable, and qualitatively the same for experiments performed over a range of N (with $\hat{W}_e = 2$), in particular it is maintained even when $N^2 = 4.4\,\text{s}^{-2}$.

It was anticipated that nonlinear decelerations of the container would result in an unstable distribution of centrifugal and pressure forces, resulting in the unsteady formation of toroidal vortices in the boundary layer. Obviously, since the redistribution of angular momentum is through an overturning motion, it may be expected that the centrifugal mechanism in a stably stratified fluid will be inhibited (at sufficiently large Burger numbers) as work has to be done in the movement of fluid against the restoring buoyancy force. In connection with these ideas an evolution to a growing boundary-layer state can be found for N^2 sufficiently large and $\hat{W}_e \approx 1$ (but still greater than unity), that is, for flows in which the T–G effect is minimized. In figure 13 we present one such example. During the experiment summarized by the figure some slight transient three-dimensional motion could be observed in the boundary layer. At somewhat larger values of $\hat{W}_e$ and/or lower Brunt-Väisälä frequencies, the quantitative agreement was lessened considerably until the centrifugal instability was dominant near the container wall and an obvious non-axisymmetric flow pattern could be observed at larger times. Figure 14 is given for comparison (this experiment
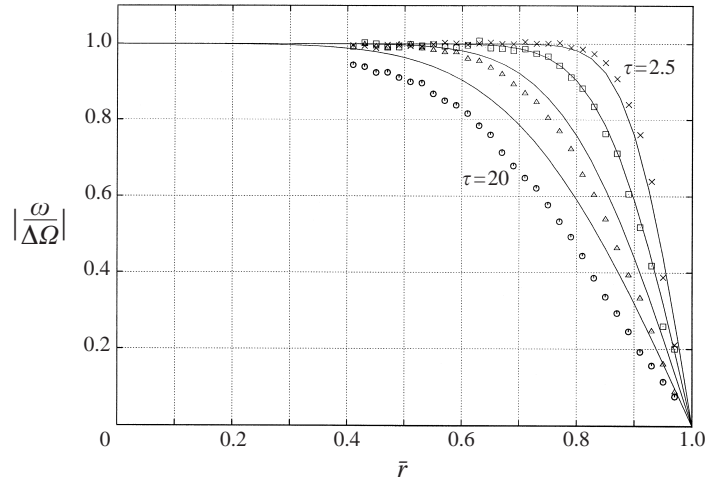
FIGURE 13. A comparison between experiment and boundary-layer analysis predictions at $\tau = 2.5, 5, 10, 20$. $\Delta\Omega = |\Omega_i - \Omega_f|$, $\Omega_i = \pi/4\,\mathrm{s}^{-1}$, $\Omega_f = \pi/5\,\mathrm{s}^{-1}$ (spin-down) $N^2 = 4.4\,\mathrm{s}^{-2}$ ($\hat{W}_e = 5/4$, $S^* = 11.2 + \hat{W}_e^2$). Numerical results are obtained with $\sigma = 700$.

was performed at a larger value of $\hat{W}_e = 2$ and with a lower Brunt–Väisälä frequency), and the large divergence between the azimuthally averaged data and predictions of the axisymmetric theory is easily seen.

The presence of the T–G mechanism is obviously of some importance in the resulting flow evolution. The form of similarity solution introduced by DFH is unlikely to be appropriate for a flow involving these vortices. If we consider the simpler problem of an axisymmetric rotating flow of an inviscid, homogeneous fluid, then Rayleigh's criterion predicts instability when the angular momentum is a decreasing function of the distance from the axis of rotation. Therefore, in a conical geometry, it is possible that the criterion could be satisfied only beyond some radial distance from the apex, and thus the similarity solution (which removes the radial dependence) is not capable of describing this behaviour.

Great care has been taken to ensure that the level of non-axisymmetry in the experimental apparatus is minimized; in none of the spin-up experiments (that is, $0 < \hat{W}_e < 1$) was there any evidence of a divergence from an axisymmetric flow. For homogeneous spin-down experiments, the centrifugal instability was obviously still present; however, there was no obvious sustained non-axisymmetry of the form found in experiments utilizing stratified fluids.

A qualitative description of a typical flow resulting from a nonlinear spin-down experiment with $1\,\mathrm{s}^{-2} \leqslant N^2 \leqslant 5\,\mathrm{s}^{-2}$ is as follows.

   (i) The rotation rate is altered via a linear deceleration, from Ω_i to $\Omega_f < \Omega_i$, over a set interval. The method of deceleration has no qualitative effect on the resulting flow providing that the change is over a timescale that is small compared to that required for a global readjustment. We use a linear ramping of the rotation merely for experimental convenience, since it minimizes any unwanted tank oscillation and shows the appearance of the three-dimensional flow more clearly.

   (ii) The centrifugal instability begins to dominate the flow near the boundary, with obvious three-dimensional motion. This stage can occur prior to the container attaining its final rotation rate $\Omega = \Omega_f$, that is, during the deceleration phase.
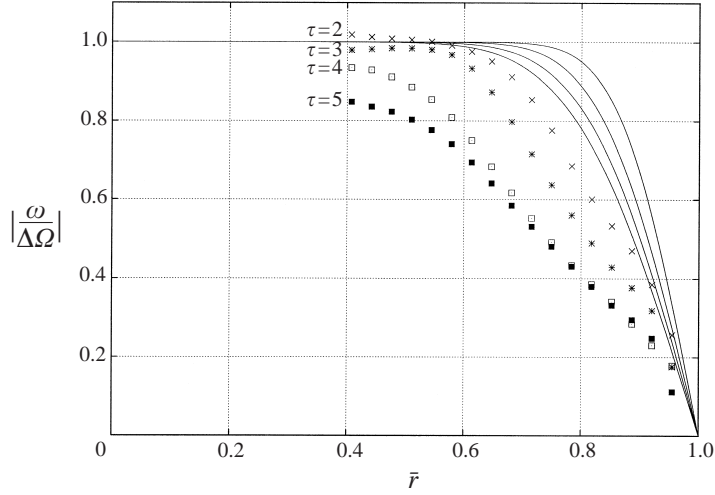
FIGURE 14. A comparison between experiment and boundary-layer analysis predictions at $\tau = 2, 3, 4, 5$. $\Delta\Omega = |\Omega_i - \Omega_f|$, $\Omega_i = \pi/5\,\mathrm{s}^{-1}$, $\Omega_f = \pi/10\,\mathrm{s}^{-1}$ (spin-down) $N^2 = 2.5\,\mathrm{s}^{-2}$ ($\hat{W}_e = 2$, $S^* = 26 + \hat{W}_e^2$). Numerical results are obtained with $\sigma = 700$, and the experimental results are an azimuthal average. In this case the axisymmetric boundary-layer analysis fails to give even qualitative information.

(iii) After a sustained T–G phase the three-dimensional motion begins to decay, with the emergence of a more regular non-axisymmetric flow.

(iv) Particle streaks in the non-axisymmetric flow can be followed in most of the light sheet over timescales that are comparable with the background rotation period. There is little obvious evidence of any associated large-scale, strong, three-dimensionality. Experiments have been performed with continuously stratified fluids with a fluorescent dye introduced into the lower half. The light sheet when placed slightly above the dye interface reveals any up-welling of denser fluid as bright regions in the field of view. Spin-down experiments of this type suggest that the non-axisymmetry can be related to localized regions of fluid (which are advected with the overall azimuthal flow) that are drawn upwards during the spin-down readjustment. We cannot determine from such experiments if the dyed region is associated with a continued up-welling or merely a sustained displacement of dyed fluid. However, localized regions of low velocity can appear near the boundary in particle tracking results, and may be associated with the same flow characteristics visualized by the dye.

(v) In some cases a region of reverse flow can also be observed near to the boundary (reverse in the sense of counter-rotation relative to the frame of reference rotating with the container).

(vi) At large times the particle streaks near the axis of the container become elliptical (displaced by the now large non-axisymmetric region near the container wall). The region of smallest fluid velocity (i.e. the centre of the elliptical particle streaks) moves away from the axis of the cone, beginning to slowly precess about it.

(vii) Eventually all non-axisymmetric behaviour begins to slowly decay leaving a residual azimuthal motion. The spin-down process is then completed over a diffusive timescale.

(viii) Once a flow approximating rigid-body motion has been attained, density measurements generally reveal that, although there may have been some mixing near
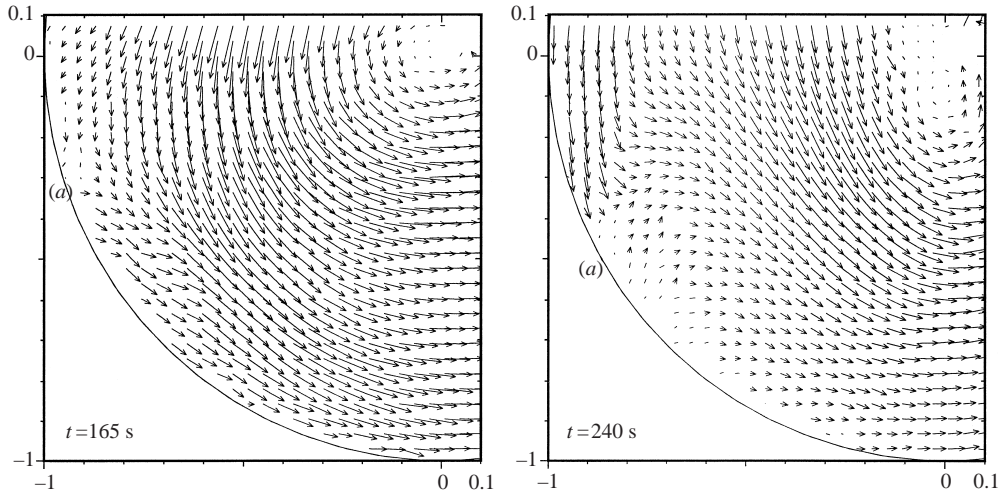
FIGURE 15. Two typical velocity fields for a spin-down experiment at $N^2 = 2.5\,\text{s}^{-2}$, with $\Omega_i = \pi/5\,\text{s}^{-1}$, $\Omega_f = \pi/10\,\text{s}^{-1}$ ($\hat{W}_e = 2$, $S^* = 6.3 + \hat{W}_e^2$). In each figure (*a*) denotes a flow feature that develops in a continuous manner from that shown in the left-hand figure to that shown on the right.

the free surface (i.e. at large radial distance from the apex), at the mid-container levels typically examined during an experiment there is little difference in the density stratification (see figure 5). This suggests that there is little vertical mixing associated with the sustained non-axisymmetric flow phase.

In figure 15 we present two typical sections of the velocity field data obtained from particle tracking in the cross-section plane over a period of 1 s ($164.5\,\text{s} \leqslant t \leqslant 165.5\,\text{s}$, and $239.5\,\text{s} \leqslant t \leqslant 240.5\,\text{s}$), for $N^2 = 2.5\,\text{s}^{-2}$. The axes of the figures are a rectilinear coordinate system that has been non-dimensionalized with the light sheet radius h, and the intersection of the light sheet with the container wall is shown as the (solid line) arc; see figure 3. The vectors shown in the figure have been scaled such that the dimensional fluid velocity is given by $4l/3$ (h/s), where l is the arrow length.

The vector fields clearly show a divergence from an axisymmetric flow and the region (*a*) denotes the same feature, which develops in a continuous manner over the timescale spanned by the two figures. This flow feature has travelled around the container several times in the interval $165\,\text{s} < t < 240\,\text{s}$. These results are qualitatively representative of non-axisymmetric evolutions obtained over the range $1\,\text{s}^{-2} < N^2 < 5\,\text{s}^{-2}$ with $\hat{W}_e = 2$.

For $\hat{W}_e \gg 1$ and moderate density stratification, the subsequent evolution of the flow is dominated by three-dimensional effects and appears to have some transition to a turbulent flow at locations sufficiently far from the apex of the cone. The final state in these cases is obviously still a rigid-body rotation at the new angular frequency Ω_f.

We conclude this section by noting that some detailed issues with regard to the spin-down of the cone are unresolved. It is quite clear that physical processes, namely Taylor–Görtler instabilities that occur first in a non-axisymmetric, non-similar lower-wall boundary layer, make any detailed comparison with the theories presented here meaningless. Though a complete, detailed, quantitative description of that process, and in particular the specific time-history of the development of the non-centred eddy seen in the fluid core, has not been established, the fact remains that we have established in the laboratory a clear distinction between spin-up and spin-down cases.
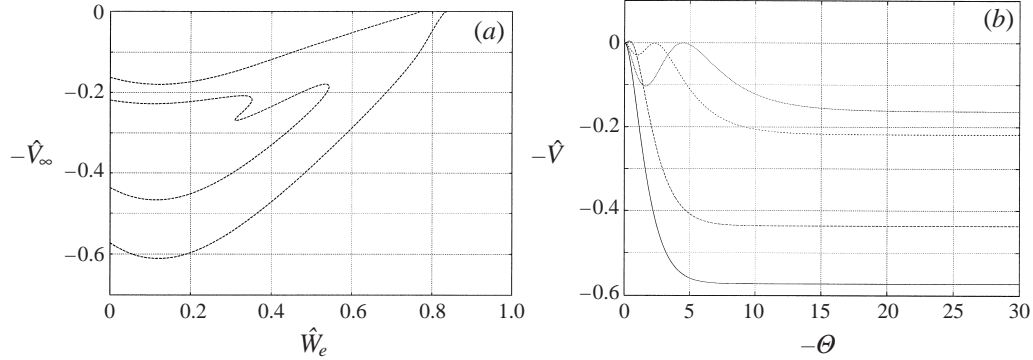
FIGURE 16. (*a*) Steady states for $S^* = \hat{W}_e^2 + 0.4$, $\sigma = 700$. These parameter values correspond to a fixed (stable) stratification, final rotation rate Ω_f, and a range of initial rotation rates from $\Omega_i = 0\,\mathrm{s}^{-1}$ ($\hat{W}_e = 0$) to $\Omega_i = \Omega_f$. (*b*) Profiles of $-\hat{V}(\Theta)$ for those points at $\hat{W}_e = 0$ shown in (*a*).

Further theoretical description of spin down is far beyond the scope of this paper, and is relegated to some future work.

5. Non-uniqueness and stability of the steady-state boundary layer

5.1. *Steady solutions*

Solving the governing steady equations numerically suggests that there is a critical Burger number, $S^*_{crit}(\hat{W}_e; \sigma)$, beyond which steady solutions cannot be located; S^*_{crit} was calculated by DFH for $\sigma = 1$. It is this boundary that defines the region in parameter space within which steady states are achieved by the initial value problem (see figure 1). An asymptotic description in the neighbourhood of S^*_{crit} is possible, providing a two-layer description of the steady solution.

In figure 16(*a*) we show several steady solutions for physically relevant parameter values, with the state characterized by the velocity normal to the wall at the boundary layer edge, $\hat{V}_\infty$. Here, $\hat{V}_\infty = \hat{V}(\Theta \to -\infty)$ as defined in §4. For the parameter values of figure 16 the branch that is achieved by an unsteady evolution from an initial state of rigid body rotation is that with the largest value of $|\hat{V}_\infty|$. Figure 16(*b*) shows profiles of $\hat{V}$ for each of the four states shown in figure 16(*a*) at $\hat{W}_e = 0$.

Since there is a multiplicity of available steady states for the boundary-layer equations it seems sensible to address the stability of the states. The existence of several stable steady solutions in sub-regions of parameter space could have implications for the unsteady development of the boundary layer.

5.2. *Numerical determination of the instability modes*

The non-dimensionalized boundary-layer equations governing spin-up/down in a conical container are as given by DFH,

$$\frac{\partial \hat{U}}{\partial t} + \hat{U}^2 + \hat{V}\frac{\partial \hat{U}}{\partial \Theta} - \hat{W}^2 = \frac{\partial^2 \hat{U}}{\partial \Theta^2} - B^*, \tag{5.1}$$

$$\frac{\partial \hat{W}}{\partial t} + 2\hat{U}\hat{W} + \hat{V}\frac{\partial \hat{W}}{\partial \Theta} = \frac{\partial^2 \hat{W}}{\partial \Theta^2}, \tag{5.2}$$

$$\frac{\partial B^*}{\partial t} + \hat{V}\frac{\partial B^*}{\partial \Theta} + \hat{U}B^* - S^*\hat{U} = \frac{1}{\sigma}\frac{\partial^2 B^*}{\partial \Theta^2}, \tag{5.3}$$

$$2\hat{U} + \frac{\partial \hat{V}}{\partial \Theta} = 0. \tag{5.4}$$

The velocity components $\hat{U}$, $\hat{V}$, $\hat{W}$ are as defined in §4, and B^* is a non-dimensional quantity representing the density perturbation within the boundary layer. We approach the linearized stability analysis by doing the usual decomposition,

$$\hat{U} = \hat{U}_0(\Theta) + \tilde{U}(\Theta, t), \quad \hat{V} = \hat{V}_0(\Theta) + \tilde{V}(\Theta, t), \tag{5.5}$$

$$\hat{W} = \hat{W}_0(\Theta) + \tilde{W}(\Theta, t), \quad B^* = \hat{B}_0(\Theta) + \tilde{B}(\Theta, t). \tag{5.6}$$

where $(\ )_0$ represents the steady state, and $(\tilde{\ })$ the small disturbance. We carry out the usual linearization, taking $|\tilde{U}| \ll |U_0|$ for all Θ.

The resulting linearized equations are

$$\tilde{U}_t + 2\hat{U}_0\tilde{U} + \hat{V}_0\tilde{U}_\Theta + \tilde{V}\hat{U}_{0\Theta} - 2\hat{W}_0\tilde{W} = \tilde{U}_{\Theta\Theta} - \tilde{B}, \tag{5.7}$$

$$\tilde{W}_t + 2\hat{U}_0\tilde{W} + 2\tilde{U}\hat{W}_0 + \hat{V}_0\tilde{W}_\Theta + \tilde{V}\hat{W}_{0\Theta} = \tilde{W}_{\Theta\Theta}, \tag{5.8}$$

$$\tilde{B}_t + \hat{V}_0\tilde{B}_\Theta + \tilde{V}\hat{B}_{0\Theta} + \hat{U}_0\tilde{B} + \tilde{U}\hat{B}_0 - S^*\tilde{U} = \frac{1}{\sigma}\tilde{B}_{\Theta\Theta}, \tag{5.9}$$

$$2\tilde{U} + \tilde{V}_\Theta = 0. \tag{5.10}$$

We note that when $\hat{B}_0 \equiv S^* = \hat{W}_e^2$, and $\tilde{B} \equiv 0$ (as is the case for a homogeneous fluid) the above equations reduce to the form considered in the stability analysis of Bodonyi & Ng (1984), that is, the stability of rotating disk flows.

For any branch of solution to the steady-state problem, we can follow the usual procedure for locating instability modes by writing

$$\tilde{q} = q(\Theta)e^{\Lambda t}, \tag{5.11}$$

where $\tilde{q}$ is generic for any of the quantities in (5.7)–(5.10). Substitution of (5.11) into (5.7)–(5.10) results in an eigenvalue problem for Λ, and the existence of any component of the spectrum with $\text{Re}(\Lambda) > 0$ implies that the steady state is unstable. The resulting eigenvalue problem can be considered with several different methods. A preliminary picture of the eigenvalue spectrum can be obtained by a straightforward discretization of the governing system, followed by the application of some global method.

In particular, by first using a QZ algorithm we can obtain the eigenvalue spectrum after employing a relatively coarse discretization. The results of this global approach can then be refined using a local search routine to determine the discrete modes with a sufficiently refined numerical grid. Finally, the results of the linear stability analysis can be compared with unsteady computations of the full boundary-layer equations with a suitably small perturbation applied to the steady state.

Applying this approach to the steady states shown in figure 16(*a*) reveals that only one of the states is stable (namely the solution arising from $\hat{V}_\infty = 0.5781$ at $\hat{W}_e = 0$), with the other states having at least one unstable eigenvalue.

Typically, the eigenvalue spectrum consists of both discrete and continuous parts and at general points in the parameter space the component with the largest real part can be either the discrete or continuous spectrum. In particular, by using a QZ algorithm we can obtain results such as those shown in figure 17. In computing the spectra shown in the figure, the edge conditions were applied at $\Theta = 50$, and
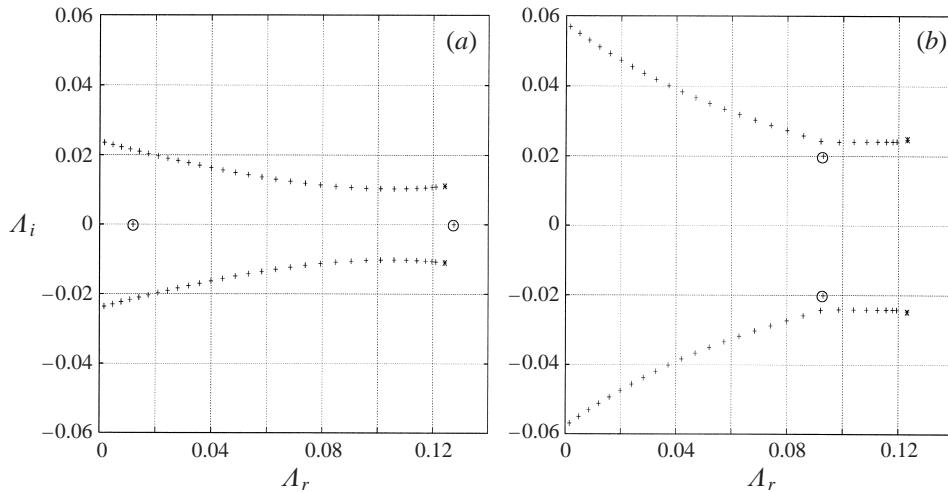
FIGURE 17. The eigenvalue spectrum obtained from applying a global method to the discretized system: (*a*) $\hat{W}_e = 0.998$, $S^* = 0.5$ and $\sigma = 700$, (*b*) $\hat{W}_e = 0.995$, $S^* = 0.5$ and $\sigma = 700$. See the text for a description of the symbols. Note that these parameter values lie in the $S^* < \hat{W}_e$ region.

401 equally spaced grid points were used in the discretization. Figure 17 shows the eigenvalues (which obviously form complex conjugate pairs) that lie in the right half-plane. We have used the notation $\Lambda = \Lambda_r + i \Lambda_i$, where $\Lambda_r > 0$ leads to a temporally growing solution. This global approach finds discrete modes (those eigenvalues that are circled) and also attempts to resolve a discretized version of a continuous spectrum. On increasing the number of grid points, the QZ algorithm becomes a computationally expensive procedure. Nevertheless, considerable variation in both the number of grid points and location at which the edge conditions are applied is required before one can be convinced that a discretized representation of the continuous spectrum is being produced. In particular, it was found that increasing the resolution would typically provide a new eigenvalue between two existing eigenvalues obtained at lower resolution. We shall examine the continuous spectrum by more analytical means in Appendix A.

On applying a local search method to track the discrete eigenvalues we find a behaviour similar to that noted in a number of Orr–Sommerfeld-type problems; see for example Murdock & Stewartson (1977), Balakumar & Malik (1992), and Mack (1976). As can be seen in figure 17(*a*), there are two discrete unstable modes (with $\Lambda_i = 0$) when $\hat{W}_e = 0.998$, $S^* = 0.5$ and $\sigma = 700$. On reducing $\hat{W}_e$ from 0.998 to 0.994 the least damped discrete mode moves along the real axis towards the origin, similarly the only other unstable discrete mode becomes more unstable, again with $\Lambda_i = 0$. At some critical value of the parameter $\hat{W}_e$ the two unstable, real eigenvalues combine to form a complex conjugate pair with $\Lambda_i \neq 0$. On decreasing $\hat{W}_e$ further the pair of eigenvalues moves away from the real axis, as shown in figure 17(*b*), and are eventually absorbed into the continuous spectrum.

This absorption of discrete modes by a continuous spectrum has been noted before. Mack (1976) considered the temporal eigenvalues of the Blasius boundary layer, and found only a finite number of discrete eigenvalues; however, on increasing the Reynolds number additional eigenvalues 'spring' from the continuous spectrum. Equivalently, eigenvalues are, in general, being absorbed by the continuous spectrum on decreasing the Reynolds number.
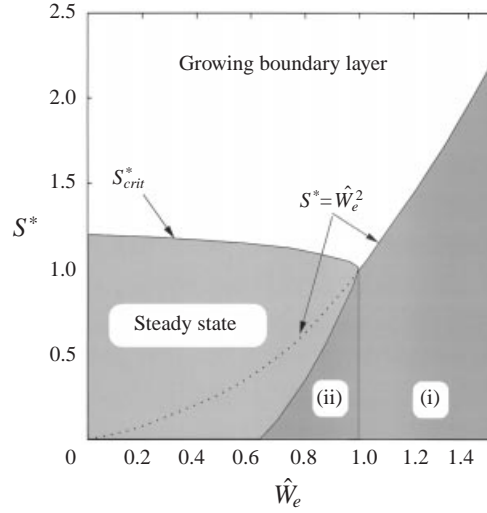
FIGURE 18. The full spin-up/down parameter space, as predicted by the axisymmetric boundary-layer theory for $\sigma = 700$. See main text for a detailed description of the regions.

It is worth noting that at some points in parameter space the discrete mode can appear to the right of the continuous spectrum in the Λ-plane, as shown in figure 17(a), and, at other points, there may be no unstable discrete modes, or it may be that there are portions of the continuous spectrum to the right of the discrete mode (figure 17b). This complicated behaviour will obviously have implications for the large-time description of the instability and we shall return to consider it in more detail in Appendix A.

The QZ algorithm is a computationally intensive method for obtaining the eigenvalues, and care is needed since it can provide spurious results. Details of the continuous spectrum can be obtained more elegantly than by direct solution of the discretized eigenvalue problem. Moreover, it is possible in some limiting cases (notably $\sigma \gg 1$, $\hat{V}_\infty \ll 1$) to obtain an approximation to the limit point of the continuous spectrum (corresponding to the location of a branch point singularity in a Laplace domain). In figure 17(a, b) we have shown the location of the branch point, as determined by this approximation (at $\Lambda_r = (\hat{W}_e^2 - S^*)/4\hat{W}_e$, $\Lambda_i = \hat{V}_\infty[(7\hat{W}_e^2 + S^*)/4\hat{W}_e]^{1/2}$), as the asterisk. A full description of the continuous spectrum, and an approximation to the location of the branch point is given in Appendix A.

As we have noted, at general points in the parameter space there can be both discrete and continuous components to the eigenvalue spectrum. However, detailed numerical investigation together with the analytical results obtained for the continuous spectrum presented in Appendix A, suggest that instability of the higher-branch steady states in $S^* > \hat{W}_e^2$ arises from the presence of unstable discrete modes in all cases (i.e. the continuous spectrum is stable). The region $S^* > \hat{W}_e^2$ (with $\sigma = 700$, and $0 < \hat{W}_e < 1$) is the area of parameter space appropriate to the laboratory experiments (as discussed in §2.1), and at general parameter values within this region a numerical investigation of the steady states and their stability indicates that at most one stable state exists. All other steady solutions relevant to the laboratory work have at least one unstable discrete eigenvalue. Unsteady computations of the nonlinear boundary-layer equations, from an initial state that is a small perturbation of a higher-branch

steady solution, evolve to the one existing stable branch, and it is this state that is obtained in the initial value problem for spin-up, $0 < \hat{W}_e < 1$.

Figure 18 shows the $(S^*, \hat{W}_e)$-plane for $\sigma = 700$, with the parameter values leading to different large-time solution characteristics clearly marked. This figure is obtained from the axisymmetric boundary-layer theory, and differs from that presented in figure 1 since it is obtained for $\sigma = 700$ (the appropriate value for a saline solution) rather than $\sigma = 1$, as discussed by DFH. The main difference of relevance to the laboratory work is the reduction in size of the region leading to steady boundary-layer states in figure 18 compared to that shown in figure 1. The region marked (i) in figure 18 is equivalent to the finite-time breakdown region shown in figure 1. The region marked (I) in figure 1 denotes stable steady states that are not achieved by an evolution from an initial state of rigid-body rotation; no such states exist at larger values of the Schmidt number and this region is absent in figure 18. Finally, region (ii) in figure 18 is an area of parameter space for which the primary branch of steady states is unstable and the initial value problem at these values leads to a new variety of finite-time breakdown as described in Appendix B. This unstable region does not extend to those parameter values relevant to the laboratory experiments ($S^* > \hat{W}_e^2$); however the other steady boundary-layer states that can be found for ($S^* > \hat{W}_e$) have been shown to be unstable by the same stability analysis.

6. Conclusions

We have examined the readjustment of a linearly stratified fluid in a conical container, making comparisons between experimentally gathered data and the previous theoretical predictions of DFH. We have observed a good quantitative agreement between the experimental data and theoretically predicted values (even for nonlinear changes in the rotation rate) when the boundary layer is sufficiently thin, and when the flow is not undergoing a nonlinear spin-down.

The previous analysis of the governing boundary-layer equations by DFH predicted both evolution to a steady state (in an infinite geometry) and temporal growth of the boundary layer into the interior; these scenarios have been confirmed experimentally. Implicit in the predictions of the theoretical work is that, eventually, the growth of the viscous region will be sufficient to render the boundary-layer approximation quantitatively inaccurate. Similarly, the experimental data have to be interpreted in terms of the finite size of the container in some regions of the parameter space, notably when a significant Ekman mass transport is predicted. Obviously, in a finite geometry recirculation of fluid transported in the boundary layers must occur.

The details of the global spin-up of fluid in such a conical container have not been presented here. Even for the case of a small-Ω change in a homogeneous fluid this geometry presents some new challenges owing to the absence of sidewall layers in the usual sense. The mechanism for stratified spin-up with small changes in Ω appears to be that discussed by Walin (1969) and Spence *et al.* (1992). However, the nonlinear case is more problematic. Provided the spin-up occurs with the boundary-layer parameters in the 'Steady State' region of figure 1, the mechanism appears to be essentially that of the linearized situation: owing to a mismatch in flux of fluid in the layer on the sloping wall and in the free-surface boundary layer, an eruption occurs in the upper corner of the container where those layers meet. That erupting fluid, with its larger angular momentum, enters the interior of the cone, but stratification effects distribute that momentum differentially in height. Only on a diffusive timescale, $O(E^{-1}\Omega^{-1})$, is that angular momentum made uniform in height, completing the spin-

up. However, for spin-up (or spin-down for that matter) with parameters in other regions of figure 1, the way in which the boundary layer imparts its new angular momentum to the fluid bulk, and the timescale over which that happens, is much less clear and is the subject of future work.

At least for some range of parameters, our experimental investigation of the flow readjustment for a nonlinear spin-down has shown the evolution to be (initially) dominated by a Taylor–Görtler instability in the boundary layer, followed by a sustained non-axisymmetric phase. A regime diagram is complex to produce for these cases since the flow is difficult to visualize, and there is a dependence on the light sheet level, half-angle of the container, stratification and size of rotation change. Further analysis of this intriguing flow regime is the subject of future work.

An analysis of the unsteady formation of these T–G vortices is extremely difficult. For homogeneous fluids in simpler geometries energy methods have been applied with some success to spin-decay flows in an attempt to provide sufficient conditions for global stability; see, for example, Neitzel & Davis (1980). Later work has dealt with similar spin-down problems numerically using finite-difference simulations of the Navier–Stokes equations for a variety of aspect ratios and Reynolds numbers; see, for example, Neitzel & Davis (1981) and Valentine & Miller (1994). A related numerical investigation of the endwall boundary layers during the spin-down process has also been given by Lopez & Weidman (1996).

The transient problem has not been considered for general geometries or stratified flow; however, the 'Taylor vortex flow' between conical cylinders (rotating at a fixed rate) has been discussed experimentally for a homogeneous fluid by Wimmer (1995). In contrast to the simpler geometry of circular Couette flow this system exhibits regions of both sub- and super-critical flow within the annular region, and, as well as the typical toroidal vortices, helical modes are also possible. Similarly, a possible relevance to equatorial jet formation prompted an experimental investigation and a linear stability analysis of stratified circular Couette flow by Boubnov, Gledzer & Hopfinger (1995). In particular, it was shown that the sustained vortex motion driven by the differentially rotating cylinders leads to the formation of discrete layers in the density profile. (It should be noted that the problem of stratified Couette flow in circular cylinders has a formal similarity to rotating Bénard convection, as discussed by Veronis 1970.)

To make any progress in investigating the processes involved in this part of the parameter space it seems likely that some combination of the methods discussed above must be applied. In particular, an experimental investigation similar to that performed by Wimmer, but with a continuously stratified working fluid may improve our understanding of the interaction between the T–G mechanism and buoyancy forces in this geometry. However, as we have already noted, it is not clear that the centrifugal instability is directly related to the eventual non-axisymmetric flow observed in the experiments. Therefore, in connection with this latter stage of the evolution, it may be instructive to reconsider the boundary-layer problem for the similarity form discussed by DFH, but with the azimuthal terms included (the similarity form can still be applied with an azimuthal dependence). It must be noted however, that in the framework of the similarity solution, any azimuthal dependence obviously remains independent of the radial coordinate. If no similarity between experiments and the numerical work can be found however, it could be that the non-axisymmetric evolution is associated with a more general radial dependence (perhaps initiated by the vortex motion), which would complicate the numerical task considerably.

It was anticipated, and subsequently shown with numerical solutions, that a large degree of non-uniqueness should be present for the steady boundary-layer equations.

We have considered the linear stability of the available steady states, and shown through a combination of different numerical approaches and analytical work that at parameter values appropriate to the laboratory work that at most one stable state exists. All higher-branch states have at least one unstable discrete eigenvalue. Although the eigenvalue spectra obtained in the linear stability analysis have been shown to have a continuous part, numerical work together with Appendix A suggests that this instability mechanism is not active (the continuous spectrum is stable) for the parameter values investigated by the laboratory experiments.

We should note that when considering the stability of rotating disk flows (or equivalently the boundary-layer system that we present here) there are essentially two different approaches. The first approach, which is the one we have taken in this work, is to consider unsteady flows of the same similarity form. The second approach assumes a steady flow in the appropriate similarity form and then considers the linearized equations of motion governing three-dimensional perturbations to this basic state. Although not a strictly rational mathematical procedure (unlike our approach) this latter technique has been widely applied to rotating disk problems, motivated in some cases by similarities to the flow found over swept wings, and in others as simply an example of a three-dimensional boundary layer. Considerable effort has been applied to making comparisons between the theoretical predictions and experimental results, see for example Gregory, Stuart & Walker (1955), Tatro & Mollö-Christensen (1967), and Wilkinson & Malik (1985). More recently Lingwood (1996, 1997) has considered the absolute instability of a family of rotating flows, obtaining results that are consistent with experimental observations of the onset of laminar–turbulent transition. Therefore, it must be remembered that when we refer to a flow as being stable/unstable, we mean within the framework of the assumptions made concerning the form of disturbance.

Finally, we should note that the parameter space for a Schmidt number of unity, as determined by DFH and reproduced in figure 1, has no region within which the primary branch of steady solutions is unstable. Therefore, the fact that the steady solutions represented by the shaded region (denoted by I, in figure 1), as shown in the parameter space diagram, are not obtained by any time-dependent process cannot be attributed to an instability of this branch of solution.

In Appendix B we have returned to the general boundary-layer problem in an unrestricted parameter space. Only a sub-region ($S^* > \hat{W}_e^2$) of this space is directly relevant (in a global sense) to the experimental investigations we have described. The aim of this work was to complete the analysis of the broader class of boundary-layer behaviour, as presented by DFH, allowing for the effects of a high Schmidt number, σ. Computational solution of the governing equations at large values of σ (initially motivated by the experimental work) has revealed a further general class of evolution. We have shown that the new evolution can be associated with a rather complex stability problem in which the presence of continuous spectra (as well as discrete modes) plays an important role. The analysis has many similarities to stability problems derived for other, rather different, boundary-layer flows; see for example Mack (1976), Balakumar & Malik (1992).

Appendix A. The continuous spectrum

It has been shown by Grosch & Salwen (1978) and Salwen & Grosch (1981) that, for the Orr–Sommerfeld equation, there may be a continuous spectrum in addition to the discrete spectrum, in a flow defined on a semi-infinite domain, and they provide an indication about how one might find that portion of the time response of the system. We follow the broad outlines of their suggestions, but some of the details are different here.

We begin by taking the Laplace transformation of (5.7)–(5.10), which leads to (5.7)–(5.10) with $\partial/\partial t$ in each equation replaced by the Laplace variable s, and initial conditions on the right-hand side. If the disturbances are taken to occur only at $\Theta = 0$, then the system remains homogeneous. Symbolically, if $\boldsymbol{f}$ denotes the vector $(\tilde{U}, \tilde{V}, \tilde{W}, \tilde{B})^{\mathrm{T}}$, and G denotes the spatial operator in (5.7)–(5.10), then (5.7)–(5.10) may be written as $\boldsymbol{f}_t + G\boldsymbol{f} = \boldsymbol{0}$ and so the Laplace transform leads to

$$s\mathscr{L}\{\boldsymbol{f}\} + G\mathscr{L}\{\boldsymbol{f}\} = \boldsymbol{0}, \tag{A 1}$$

where $\mathscr{L}\{q\}$ is the Laplace transform of q. Grosch & Salwen indicate that the continuous spectrum may be determined by examining the large-$|\Theta|$ behaviour of the solutions to (A 1). We do this by writing $\mathscr{L}\{\boldsymbol{f}\} = \boldsymbol{C}\exp(\lambda\Theta)$, which leads to a sixth-order polynomial whose solutions give the large-$|\Theta|$ behaviour of $\mathscr{L}\{\boldsymbol{f}\}$. Note that $\boldsymbol{C} = \boldsymbol{C}(s)$, and that function cannot be determined unless the detailed connection to the lower layer and the initial conditions are known. We return to this point later in discussing the large-t approximations to the inversion integral.

The polynomial determining λ may be written as

$$(s + \hat{V}_\infty\lambda - \lambda^2/\sigma)[(\lambda^2 - \hat{V}_\infty\lambda - s)^2 + 4\hat{W}_e^2] + 2\kappa(\lambda^2 - \hat{V}_\infty\lambda - s) = 0, \tag{A 2}$$

$$\kappa \equiv \tfrac{1}{2}(\hat{W}_e^2 - S^*), \tag{A 3}$$

where $\hat{V}_\infty$ and $\hat{W}_e$ are the values of $\hat{V}_0$ and $\hat{W}_0$ at the edge of the layer.

A.1. *The case $\sigma \equiv 1$*

In this case, equation (A 2) takes a simpler form that is easily solved, namely

$$(s + \hat{V}_\infty\lambda - \lambda^2)[-2\kappa + (\lambda^2 - \hat{V}_\infty\lambda - s)^2 + 4\hat{W}_e^2]. \tag{A 4}$$

The six roots are then given by

$$\lambda_{1,2} = -\tfrac{1}{2}\hat{V}_\infty \pm \left(\tfrac{1}{4}\hat{V}_\infty^2 + s\right)^{1/2}, \tag{A 5}$$

$$\lambda_{3,4,5,6} = \tfrac{1}{2}\hat{V}_\infty \pm \left\{\tfrac{1}{4}\hat{V}_\infty^2 + s \pm \mathrm{i}\left(4\hat{W}_e^2 - 2\kappa\right)^{1/2}\right\}^{1/2}. \tag{A 6}$$

Note that the three roots with positive real part necessary to form a solution give a function which has branch point singularities in the Laplace (s) domain. In particular, such branch points are indicative of a continuous spectrum, since the Laplace inversion path must be deformed about a branch cut starting at each such branch point and running to the left, parallel to the real axis. Here, the three branch points are of the square-root variety, and their locations are at

$$s = -\hat{V}_\infty^2/4, \quad s = -\hat{V}_\infty^2/4 \pm \mathrm{i}(4\hat{W}_e^2 - 2\kappa)^{1/2}. \tag{A 7}$$

Since these branch points all lie in the half plane $\mathrm{Re}(s) < 0$, the continuous spectrum is stable and of no real importance to time-developing instabilities. Notice that at each branch point there is a double root for λ.

This section deals with a limiting case of some importance, since in many situations the value of $\hat{V}_\infty$ is quite small and σ is large. This case is also directly relevant to the trivial solution available at $\hat{W}_e = 1$. Simply setting $\hat{V}_\infty$ and $1/\sigma$ to zero in (A 2) simplifies the polynomial to

$$(\lambda^2 - s)^2 + \frac{2\kappa}{s}(\lambda^2 - s) + 4\hat{W}_e^2 = 0. \tag{A 8}$$

The four roots are then

$$\lambda_{1,2,3,4} = \pm\left\{ s - \frac{\kappa}{s} \pm \left(\frac{\kappa^2}{s^2} - 4\hat{W}_e^2 \right)^{1/2} \right\}^{1/2}, \tag{A 9}$$

with the two $\pm$ taken independently, leading to four roots. There are, of course, two others corresponding to large but finite σ, but they are of no importance to the stability of the flow. There are branch points at the zeros of the inner square root, the most important being the one in the right half-plane that is given by

$$s_o = \frac{\kappa}{2\hat{W}_e} = \frac{\hat{W}_e^2 - S^*}{4\hat{W}_e}, \tag{A 10}$$

and there are also square-root singularities at two other locations, namely on the imaginary axis, at $s = \pm \mathrm{i}(4\hat{W}_e^2 - 2\kappa)^{1/2}$, which leads to an algebraically decaying, oscillatory component of the solution. Clearly, underneath the limiting curve $S^* = \hat{W}_e^2$, this branch point is always in the right-half-plane, leading an unstable, continuous spectrum for this instability. It is important for a computational strategy, that at the branch point, the four roots become only two; that is, there are two double roots. Also notice that for this case, at the branch point, the values of λ are given by

$$\lambda_o = \pm \mathrm{i}\left(\frac{S^* + 7\hat{W}_e^2}{4\hat{W}_e} \right)^{1/2}. \tag{A 11}$$

This result agrees with the statement of Grosch & Salwen (1978) that the value of λ on the branch cut should be pure imaginary. At more general parameter values however, the value of λ has both real and imaginary parts.

A.3. *Branch point locations for the general case*

Obviously, for non-zero values of $1/\sigma$ and $\hat{V}_\infty$, it is impossible to solve (A 2) for $\lambda(s)$. However, note that in the previous cases, at a branch point location, there is a double root for λ. Hence, whereas it is impossible to obtain complete expressions for roots, we can obtain the branch point locations. At a double root, the λ derivative of (A 2) must also be satisfied. Differentiating (A 2) with respect to λ leads to

$$((\lambda^2 - \phi)^2 + 4\hat{W}_e^2)\phi + 2\kappa(\lambda^2 - \phi) = \frac{\lambda^2}{\sigma}((\lambda^2 - \phi)^2 + 4\hat{W}_e^2), \tag{A 12}$$

$$2\lambda\phi[\kappa + \phi(\lambda^2 - \phi)] = \left(\hat{V}_\infty - \frac{2\lambda}{\sigma} \right)\kappa(\lambda^2 - \phi) + (\hat{V}_\infty - s\lambda)\left(\frac{\lambda^2}{\sigma} - \phi \right)(\lambda^2 - \phi)\frac{\lambda^2}{\sigma}$$
$$- \left[\frac{\hat{V}_\infty \lambda^2}{\sigma} - \frac{2\lambda^3}{\sigma} - \hat{V}_\infty \phi \right][\kappa + \phi(\lambda^2 - \phi)], \tag{A 13}$$

where

$$\phi \equiv s + \hat{V}_\infty \lambda. \tag{A 14}$$

Simultaneous solution of these equations locates the branch point and the corresponding value of the double root. Setting $\sigma = \infty$ and $\hat{V}_\infty$ to zero recovers the results in §A.2 above. The reader is cautioned that the dependence of the branch point locations on S^*, σ, and $\hat{W}_e$ is even more complicated than it appears here, because $\hat{V}_\infty$ is itself a complicated function of those three variables, whose value must be obtained numerically from the steady-state computation for a given set of $\{S^*, \hat{W}_e, \sigma\}$.

Large σ and small $\hat{V}_\infty$

Note that, as written, the right-hand sides of (A 12) and (A 13) constitute the corrections to (A 10) and (A 11) for non-zero values of $1/\sigma$ and $\hat{V}_\infty$. If we insert an expansion in powers of $\hat{V}_\infty$ and σ^{-1} into these equations, the result is that

$$\phi \sim s_o + \frac{\lambda_o^2}{\sigma} + O(\sigma^{-2}, \hat{V}_\infty^2), \tag{A 15}$$

$$\lambda \sim \lambda_o - \frac{\kappa^2 \hat{V}_\infty}{4\phi_o^2(\phi_o^2 - \kappa)} + \frac{\lambda_o}{4\sigma} \frac{\kappa^2 - \kappa\phi_o^2 + \phi_o^4}{\phi_o^2(\phi_o^2 - \kappa)} + O(\hat{V}_\infty^2, \sigma^{-2}), \tag{A 16}$$

using the notation of (A 10) and (A 11). Tacit in this approximation is the assumption that $\sigma^{-1} = O(\hat{V}_\infty)$, and since $\hat{V}_\infty$ is typically $O(10^{-1})$, this approximation is not necessarily valid for σ values beyond 10 or so, since terms $O(\hat{V}_\infty^2)$ should then to be retained. It is also evident from (A 12) and (A 13) that if κ is small, a new approximation must be utilized, so in fact we require that $\hat{V}_\infty = o(\kappa)$ as well.

Equations (A 15) and (A 16) may be rearranged to give the location of the two right-most branch points in this limiting case as

$$s = \frac{1}{4\hat{W}_e}\left[\left(1 - \frac{7}{\sigma}\right)\hat{W}_e^2 - \left(1 + \frac{1}{\sigma}\right)S^*\right] \pm i\hat{V}_\infty\left(\frac{S^* + 7\hat{W}_e^2}{4\hat{W}_e}\right)^{1/2} + O(\hat{V}_\infty^2, \sigma^{-2}, \hat{V}_\infty^2/\kappa). \tag{A 17}$$

This result suggests that the flow will be stable (ignoring any discrete modes for the moment) at sufficiently small values of σ, specifically for $\sigma < (7\hat{W}_e^2 + S^*)/(\hat{W}_e^2 - S^*)$. This result must be used with care since its validity depends on the satisfaction of the various ordering criteria.

Large-σ branch point locations

In the laboratory, σ is about 700, so it makes sense to examine solutions of (A 12) and (A 13) for $\sigma \to \infty$. After some algebra, (A 12) and (A 13) can be combined into a single equation for ϕ, and a second that allows computation of the corresponding λ,

$$\bar{\kappa}\Phi^{3/2}(\Phi^2 - 1)^{1/2}\{1 - \bar{\kappa}\Phi^2 \pm (1 - \Phi^2)^{1/2}\}^{1/2} = \frac{\hat{V}_\infty}{(8\hat{W}_e)^{1/2}}[1 \pm (1 + \bar{\kappa}\Phi^2)(1 - \Phi^2)^{1/2}], \tag{A 18}$$

$$\lambda = \pm\left\{\frac{2\hat{W}_e}{\Phi}\left[\pm(1 - \Phi^2)^{1/2} + \bar{\kappa}\Phi^2 - 1\right]\right\}^{1/2}, \quad \Phi \equiv \frac{2\hat{W}_e}{\kappa}\phi, \quad \bar{\kappa} \equiv \frac{\kappa}{4\hat{W}_e^2}. \tag{A 19}$$

The above form for λ leads to the same four branch points noted in §A.2, in a different notation. It is evident from this expression for Φ that, even if $\hat{V}_\infty$ is small, one cannot discard the right-hand side of (A 17) near the curve $\bar{\kappa} = 0$. If we are sufficiently far removed from that curve, so that $\hat{V}_\infty/\bar{\kappa} \ll 1$, we can obtain an approximate solution

for Φ for the right-hand branch points, in the form,

$$\Phi \sim 1 + \frac{\hat{V}_\infty^2}{16\hat{W}_e^2\bar{\kappa}^2(1-\bar{\kappa})}, \quad \hat{V}_\infty \to 0. \tag{A 20}$$

and the value of λ there is

$$\lambda \sim \lambda_o + \frac{1+\bar{\kappa}}{4\bar{\kappa}(1-\bar{\kappa})}\hat{V}_\infty + O(\hat{V}_\infty^2). \tag{A 21}$$

Eventually, after some work, we find that the branch point locations are given, to two orders in $\hat{V}_\infty$, as

$$s = \lambda_o\hat{V}_\infty + \frac{\kappa}{2\hat{W}_e}\left[1 + \frac{3}{32}\frac{\hat{V}_\infty^2}{\hat{W}_e^2\bar{\kappa}^2(1-\bar{\kappa})}\right] + O(\hat{V}_\infty^3). \tag{A 22}$$

It is worth noting that unlike the Orr–Sommerfeld cases discussed by Grosch & Salwen (1978) the values of the roots, λ, are not pure imaginary at the branch points.

A.4. *A numerical criterion*

The above procedure can only be followed analytically for the limiting cases given; we require a numerical procedure for locating the branch points at general values of the parameters. This can be done quite easily by using any standard routine capable of finding the roots of the sixth-degree polynomial (A 2). Note that in finding the branch points, which are apparently always square-root in nature in this problem, we set that root to zero, thereby loosing root multiplicity. Hence, a very simple procedure is to search the right half-plane for roots, then the locations where there is a double root constitute branch points. The strategy noted by Grosch & Salwen (1978) is not satisfactory here, since in our case one pair of roots is not necessarily pure imaginary on the branch cut, as is evident from examination of the above approximate results.

By adopting this numerical procedure we are able to follow the location of the branch point in the Laplace domain whilst gradually varying the location in the $\{\hat{W}_e, S^*, \hat{V}_\infty\}$ parameter space (at fixed σ). On altering the parameters slightly, we use the previously computed location as the first approximation to the branch point for the current parameters. We can begin the procedure with an approximation to the branch point provided by the above analysis or from an application of the QZ algorithm with sufficient resolution.

One feature of obvious interest that can be readily obtained by this numerical criterion is the stability boundary in parameter space beyond which the branch point moves into the right half-plane. This stability boundary is shown in figure 18 dividing the regions denoted by steady state and (ii); the location of this boundary was obtained by following only the primary branch of the steady solutions.

A.5. *The large-time behaviour*

Clearly, for the cases when $\mathscr{L}\{f\}$ has a branch point in the right half-s-plane, the Laplace inversion contour, given by the contour Γ, can be deformed into a new contour, Γ_1, which wraps around the one or two branch cuts. Then that portion of the Laplace inversion that leads to instability involves simply the integration along the segments of the branch cuts lying in $\mathrm{Re}(s) > 0$. Presumably a numerical superposition of the solutions obtained above would be one way to construct such an integral.

We now consider the large-time behaviour of the solutions at the edge of the layer for large σ and small $\hat{V}_\infty$. As an alternative to the integration on path Γ_1, the

large-time behaviour near the edge of the boundary layer can be deduced by the following steepest-descent strategy.

Of the four roots of the polynomial (A 2) that have positive real part, at large Θ, the one with smallest real part in any region of the s-plane, say λ_m, is dominant, hence

$$\mathscr{L}\{\boldsymbol{f}\} \sim \boldsymbol{C}_m e^{\lambda_m \Theta}. \tag{A 23}$$

Thus, the large-time, large-Θ behaviour of $\boldsymbol{f}$ is given by

$$\boldsymbol{f} \sim \frac{1}{2\pi i} \int_{\Gamma_1} \boldsymbol{C}_m(s) \, e^{st+\lambda_m \Theta} \, ds, \quad -\Theta \gg 1. \tag{A 24}$$

Evaluation of the cut integrals is difficult, even at large $(-\Theta)$, but really unnecessary anyway, since the large-time behaviour can be obtained by a steepest descent approach, requiring one more path deformation, to a path Γ_2. It turns out that the saddle points lie off the end of the branch cuts as shown. The saddle points are clearly given by solutions of $d\lambda_m/ds = -\Theta/t$. Let the upper location be denoted by s_c. Then, formally, provided we choose the path through the branch point to be a steepest path, and noting that the contribution from the lower point will be the complex conjugate of the upper, we have

$$\boldsymbol{f} \sim \left(\frac{1}{-2\pi\Theta}\right)^{1/2} \mathrm{Re}\left(\boldsymbol{C}(s_c) \left(\frac{1}{|\lambda_m''(s_c)|}\right)^{1/2} e^{s_c t + \lambda_m(s_c)\Theta - i(\pi/2 - \psi)}\right), \tag{A 25}$$

where ψ is the angle of the path through the saddle point, and is given by $\psi = -\arg(\lambda_m''(s_c))$. Since, in this expression $-\Theta/t = O(1)$, the general form of the solution is

$$\boldsymbol{f} \sim \frac{1}{(-\Theta)^{1/2}} \boldsymbol{F}(-\Theta/t) \cos\left(\mathrm{Im}(\lambda_m(s_c))\Theta + \mathrm{Im}(s_c)t + \boldsymbol{\Psi}\right)$$
$$\times \exp\left(\mathrm{Re}(s_c)t + \mathrm{Re}(\lambda_m(s_c))t\right). \tag{A 26}$$

While this expression is perhaps instructive, it cannot be further evaluated by asymptotic means alone because $\boldsymbol{F}$ depends on the details of the quantity $\boldsymbol{C}(s)$, whose form cannot be found.

However, if we suppose that $-\Theta/t \ll 1$, then it can be shown that the saddle point moves in close to the branch point, so that the quantity $\boldsymbol{C}(s_c)$ is given approximately by $\boldsymbol{C}(s_o)$, which is a constant independent of either Θ or t. That makes evaluation of the various quantities possible, and after considerable algebra, it can be shown that the large-time behaviour for $\sigma \gg 1$ and $\hat{V}_\infty \ll 1$ is approximated by

$$\boldsymbol{f} \sim |\boldsymbol{C}(s_o)| \left(\frac{\hat{W}_e \Theta^2}{(1-\bar{\kappa})\pi t^3}\right)^{1/2} \cos((2\hat{W}_e(1-\bar{\kappa}))^{1/2}(\Theta - \hat{V}_\infty t) + \boldsymbol{D}) e^{\kappa t/(2\hat{W}_e)},$$
$$t \gg (-\Theta) \gg 1, \quad \text{and} \quad \boldsymbol{D} = \arg(\boldsymbol{C}(s_o)), \tag{A 27}$$

for $\sigma \gg \hat{V}_\infty^{-1} \gg 1$. Similar expressions may be obtained for other limiting cases. Note that this solution does not vanish for large $(-\Theta)$, but that is a result of the restriction $-\Theta \ll t$. The solution certainly decays at large $(-\Theta)$.

The important result here is that the instability is somewhat weaker than exponential, behaving like $t^{-3/2} \exp(s_o t)$. Although we do not present the results here, we have verified the algebraic component by numerically marching the linear stability equations forward in time and comparing with the above result.
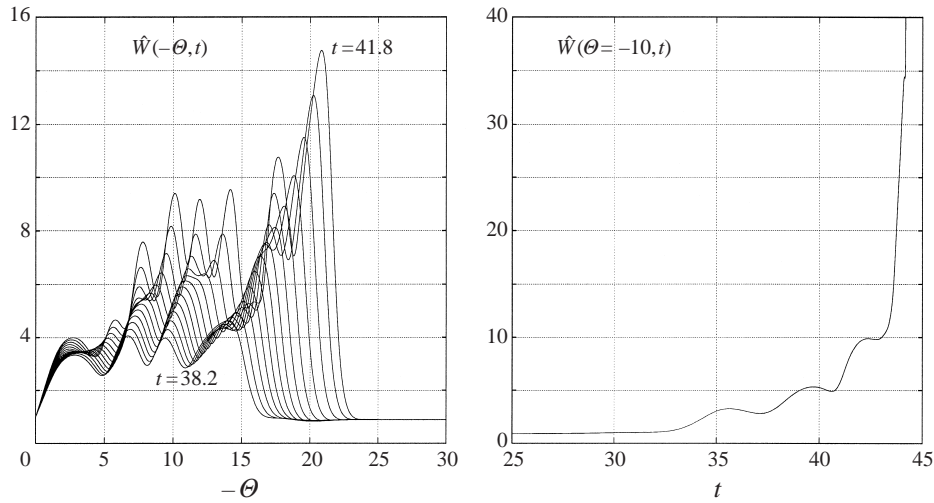
FIGURE 19. A finite-time breakdown at $S^* = 0$, $\hat{W}_e = 0.9$ and $\sigma = 700$.

Appendix B. A new finite-time breakdown

The parameter space diagram presented by DFH needs some modification for Schmidt numbers, σ, somewhat greater than unity. The numerical work of DFH was (mainly) presented for $\sigma = 1$, and it was noted that the parameter space remained largely unchanged at higher Schmidt numbers.

A preliminary investigation of the $\sigma \gg 1$ regime suggested that the boundary layer separates into a thin buoyancy layer, in which the velocity components are Taylor series expansions from a thicker velocity boundary layer. The most significant effect from the point of view of the parameter space diagram was a shift of S^*_{crit}, the boundary that separates the steady-state region from the growing boundary-layer region, to lower values of S^*.

Recently, however, numerical computations of the governing boundary-layer equations for parameter values approaching $\hat{W}_e = 1$, and at more general (larger) values of σ, have revealed an interesting new class of breakdown. A typical example of the breakdown is shown in figure 19, which shows profiles of $\hat{W}(\Theta, t)$ as $t \to t_0$ the time at breakdown. Similar results can be obtained for the other components of velocity and buoyancy.

A comparison of this figure with similar results for the finite-time singularity obtained in the $\hat{W}_e > 1$, $S^* < \hat{W}_e^2$ region (as presented by DFH†) reveals no similarities. In particular, the previously presented singular behaviour (in the case $\hat{W}_e > 1$) occurred largely within an inner region $\Theta \sim (t - t_0)^{1/2}$, whereas in this case the breakdown dominates the profiles in a region that is displaced away from the boundary, with the wall components of stress and buoyancy remaining finite. The breakdown can always be associated with an increasing (spatial) oscillatory behaviour as shown in the figure. We must note that there is some degree of assumption when referring to the results as showing a finite-time breakdown, since we have not formally connected the numerical results to any asymptotic description.

Rather than simply performing the unsteady computations over a wide range

---

† We note that there is a typographical error in the boundary condition (4.32) presented by DFH. The correct condition is $\hat{W}_1(\tilde{\eta} = 0) = 0$.

of parameters and then inferring boundaries in the parameter space within which this behaviour occurs, we can show that this evolution is associated with a linear instability of the steady states. At large σ, within the steady-state region of figure 18 there exists one stable steady-state together with, typically, a number of unstable states. The initial value problem in this region of parameter values always evolves to the one stable solution. On moving from the steady-state region to the area of parameter space denoted by (ii) however, the steady state becomes unstable and the initial value problem develops a finite-time breakdown. The stability analysis is as given in §5, but in this case the continuous component of the eigenvalue spectrum (as discussed in Appendix A) can be unstable and dominate the unstable discrete modes.

The stability problem can be discussed more formally, and it is by this approach that we can determine at what parameter values this new evolution is obtained, as shown in figure 18. Since we only consider the linear stability problem, we cannot connect the finite-time breakdown and the instability in any formal manner. However, unsteady computations at parameter values near the stability boundary in parameter space (i.e. near the boundary between the steady-state region and region(ii)) suggest that the numerical breakdown discussed above is eventually obtained after nonlinear effects supersede the linear instability.

REFERENCES

BALAKUMAR, P. & MALIK, M. R. 1992 Discrete modes and continuous spectra in supersonic boundary layers. *J. Fluid Mech.* **239**, 631.

BENTON, E. R. & CLARK, A. 1974 Spin-up. *Ann. Rev. Fluid Mech.* **6**, 257.

BODONYI, R. J. 1978 On the unsteady similarity equations for the flow above a rotating disc in a rotating fluid. *Q. Appl. Math. Mech.* **31**, 461.

BODONYI, R. J. & NG, B. S. 1984 On the stability of the similarity solutions for swirling flow above an infinite rotating disk. *J. Fluid Mech.* **144**, 311.

BODONYI, R. J. & STEWARTSON, K. 1977 The unsteady laminar boundary layer on a rotating disk in a counter-rotating fluid. *J. Fluid Mech.* **79**, 669.

BOUBNOV, B. M., GLEDZER, E. B. & HOPFINGER E. J. 1995 Stratified circular Couette-flow – instability and flow regimes. *J. Fluid Mech.* **292**, 333.

BUZYNA, G. & VERONIS, G. 1971 Spin-up of a stratified fluid: theory and experiment. *J. Fluid Mech.* **50**, 579.

DALZIEL, S. B. 1992 Decay of rotating turbulence – some particle tracking experiments. *Appl. Sci. Res.* **49**, 217.

DAVIES, P. A., FERNANDO, H. J. S., BESLEY, P. & SIMPSON, R. J. 1991 The generation and spreading of a turbulent mixed layer in a rotating stratified fluid. *J. Geophys. Res.* **96**, NC7, 12567.

DUCK, P. W., FOSTER, M. R. & HEWITT, R. E. 1997 On the boundary layer arising in the spin-up of a stratified fluid in a container with sloping walls. *J. Fluid. Mech.* **335**, 233 (referred to herein as DFH).

GARRETT, C., MACCREADY, P. & RHINES P. 1993 Boundary mixing and arrested Ekman layers: Rotating stratified flow near a sloping boundary. *Ann. Rev. Fluid Mech.* **25**, 291.

GREENSPAN, H. P. 1968 *The Theory of Rotating Fluids.* Cambridge University Press.

GREENSPAN, H. P. & HOWARD, L. N. 1963 On a time-dependent motion of a rotating fluid. *J. Fluid. Mech.* **17**, 385.

GREENSPAN, H. P. & WEINBAUM, S. 1965 On nonlinear spin-up of a rotating fluid. *J. Maths and Phys.* **44**, 66.

GREGORY, N., STUART, J. T. & WALKER, W. S. 1955 On the stability of three-dimensional boundary layers with application to the flow due to a rotating disk. *Phil. Trans. R. Soc. Lond.* A **248**, 155.

GROSCH, C. E. & SALWEN, H. 1978 The continuous spectrum of the Orr–Sommerfeld equation. Part 1. The spectrum and eigenfunctions. *J. Fluid Mech.* **87**, 33.

HOLTON, J. R. 1965 The influence of viscous boundary layers on transient motions in a stratified rotating fluid, Part I. *J. Atmos. Sci.* **22**, 402.

LINGWOOD, R. J. 1996 An experimental study of absolute instability of the rotating-disk boundary layer flow. *J. Fluid Mech.* **314**, 373.

LINGWOOD, R. J. 1997 Absolute instability of the Ekman layer and related flows. *J. Fluid Mech.* **331**, 405.

LOOPEZ, J. M. & WEIDMAN, P. D. 1996 Stability of stationary endwall boundary layers during spin-down. *J. Fluid Mech.* **326**, 373.

MACCREADY, P. & RHINES, P. B. 1991 Buoyant inhibition of Ekman transport on a slope and its effect on stratified spin up. *J. Fluid. Mech.* **223**, 631.

MACK, L. M. 1976 A numerical study of the temporal eigenvalue spectrum of the Blasius boundary layer. *J. Fluid Mech.* **73**, 497.

MURDOCK, J. W. & STEWARTSON, K. 1977 Spectra of the Orr–Sommerfeld equation. *Phys. Fluids* **20**, 1404.

NEITZEL, G. P. & DAVIS, S. H. 1980 Energy stability theory of decelerating swirl flows. *Phys. Fluids* **23**, 432.

NEITZEL, G. P. & DAVIS, S. H. 1981 Centrifugal instabilities during spin-down to rest in finite cylinders. *J. Fluid Mech.* **102**, 329.

OSTER, G. 1965 Density gradients. *Sci. Am.* **213**, 70.

PEDLOSKY, J. 1967 The spin-up of a stratified fluid. *J. Fluid. Mech.* **28**, 463.

ROGERS, M. H. & LANCE. G. N. 1960 The rotationally symmetric flow of a viscous fluid in the presence of a rotating disk. *J. Fluid Mech.* **7**, 617.

SAKURAI, T. 1969 Spin down problem of a rotating stratified fluid in thermally insulated circular cylinders. *J. Fluid Mech.* **37**, 689.

SALWEN, H. & GROSCH, C. E. 1981 The continuous spectrum of the Orr–Sommerfeld equation. Part 2. eigenfunction expansions. *J. Fluid Mech.* **104**, 445.

SPENCE, G. S. M., FOSTER, M. R. & DAVIES, P. A. 1992 The transient response of a contained rotating stratified fluid to impulsively started surface forcing. *J. Fluid Mech.* **243**, 33.

TATRO, P. R. & MOLLÖ-CHRISTENSEN, E. L. 1967 Experiments on Ekman layer instability. *J. Fluid Mech.* **28**, 531.

THORPE, S. A. 1987 Current and temperature variability on the continental slope. *Phil. Trans. R. Soc. Lond.* A **323**, 471.

VALENTINE, D. T. & MILLER, K. D. 1994 Generation of ring vortices in axisymmetric spin-down: A numerical investigation *Phys. Fluids* **6**, 1535.

VERONIS, G. 1970 The analogy between rotating and stratified fluids. *Ann. Rev. Fluid. Mech.* **2**, 37.

WALIN, G. 1969 Some aspects of time-dependent motion of a stratified fluid. *J. Fluid Mech.* **36**, 289.

WEDEMEYER, E. H. 1964 The unsteady flow within a spinning cylinder. *J. Fluid. Mech.* **20**, 383.

WILKINSON, S. P. & MALIK, M. R. 1985 Stability experiments in the flow over a rotating disk. *AIAA J.* **23**, 588.

WIMMER, M. 1995 An experimental investigation of Taylor vortex flow between conical cylinders. *J. Fluid Mech.* **292**, 205.

ZANDBERGEN, P. J. & DIJKSTRA, D. 1987 Von Kármán swirling flows. *Ann. Rev. Fluid Mech.* **19**, 465.